Received: 8 July 2022 | Revised: 23 November 2022 | Accepted: 3 January 2023

DOI: 10.1111/joa.13825

Journal of Anatomy ANATOMICAL SOCIETY WILEY

REVIEW ARTICLE

Osteohistology and palaeobiology of giraffids from the Mio-Pliocene Langebaanweg (South Africa)

Juan Marcos Jannello[1,2] | Anusuya Chinsamy[1]

[1]Department of Biological Sciences, University of Cape Town, Rhodes Gift, South Africa

[2]Instituto de Evolución, Ecología Histórica y Ambiente (IDEVEA) CONICET-UTN-FRSR, San Rafael, Argentina

Correspondence
Juan Marcos Jannello, Instituto de Evolución, Ecología Histórica y Ambiente (IDEVEA) CONICET-UTN-FRSR, Av. Gral. J. J. Urquiza 314, 5600, San Rafael, Mendoza, Argentina.
Email: marcosjnnello@hotmail.com

Funding information
DSI-NRF Centre of Excellence; National Research Foundation AOP, Grant/Award Number: 136510

Abstract

The reconstruction of life history traits, such as growth rate, age at maturity and age at death can be estimated from the histological analysis of long bones. Here, we studied 20 long bones (metapodials, tibia and femora) of *Sivatherium hendeyi* and *Giraffa* cf. *Giraffa jumae* recovered from the Miocene–Pliocene locality of Langebaanweg on the West Coast of South Africa. We analysed the long bone histology and growth marks of juvenile and adult specimens of these taxa. Our results show that bone tissue types and vascular canal orientation varies during ontogeny, as well as between the different skeletal elements, and also across single cross sections of bones. Majority of our specimens appear to be still growing, with only an adult metacarpal of *S. hendeyi* being skeletally mature as indicated by the presence of an outer circumferential layer. We propose that the growth marks preserved in the cortices of the bones studied are most likely related to multiple catastrophic events as opposed to being annual/seasonal.

KEYWORDS
giraffa, long bone histology, neogene, palaeohistology, *Sivatherium*

1 | INTRODUCTION

Studies of the bone histology of extinct and extant vertebrates have led to a better understanding of their life history traits and biology (e.g. Chinsamy-Turan, 2005, 2012; Enlow & Brown, 1958; Erickson, 2005; Padian & Lamm, 2013). More specifically, studies of mammalian bone histology have advanced substantially in the last two decades (e.g. Chinsamy & Warburton, 2021; Kolb, Scheyer, Lister, et al., 2015; Kolb, Scheyer, Veitschegger, et al., 2015; Montoya-Sanhueza et al., 2020, 2022; Nacarino-Meneses & Chinsamy, 2021; Nacarino-Meneses et al., 2021; Sanders & Andrassi, 2006).

Despite the abundance of extant ungulate species, limb bone histology has only been conducted in a few taxa and has been focused mainly on modern artiodactyls. Some studies have focused on the assessment of life history traits such as, growth patterns and size in deer and reindeer (Singh et al., 1974), comparative growth of young sheep (Cambra-Moo et al., 2015) and pigs (Mori et al., 2005), as well as on deer (Amson et al., 2015; Calderón et al., 2021; Calderón et al., 2019; Kolb, Scheyer, Lister, et al., 2015; Kolb, Scheyer, Veitschegger, et al., 2015), and more recently on *Giraffa camelopardalis* Linnaeus, 1758 (Smith, 2020). For example, Kolb, Scheyer, Lister, et al. (2015) examined body size and growth in deer, whereas Skedros et al. (1997) undertook several studies to examine the biomechanical properties of the metacarpals of equids (Skedros et al., 2003), calcanei of horses, elks and sheep (Skedros et al., 1997), as well as studies of the humerus, radius, metacarpal and phalanx of the rocky mountain mule deer (Skedros et al., 2003). However, it is only over the past decade or so, that several studies have focused

on the ontogenetic changes in the bone histology of various artiodactyls (ruminants; Jordana et al., 2016; Köhler et al., 2012, Marín-Moratalla et al., 2013); and perissodactyls (Nacarino-Meneses et al., 2016a). Interestingly, a skeletochronological study of several *Equus* species (*E. hemionus*, *E. grevi*, *E. quagga*) demonstrated the presence of a 'birth line' that is marked by a change in the orientation of the vascular canals and which is likely related to the stress of birth (Nacarino-Meneses & Köhler, 2018).

Among the ungulates, only a few studies have focused on the modern giraffe, *G. camelopardalis*. In his description of the left femur of *G. camelopardalis*, Foote (1916) noted that in the periphery to mid cortical regions of the anterior, medial and lateral parts of the compacta, bands of laminae interrupted Haversian bone tissue, whereas in the posterior and inner cortex of the medial and lateral regions Haversian bone tissue was abundant. More recently, in a study of the crystallographic organization of giant extinct and extant animals, Dumont et al. (2014), included a giraffe humerus, and although no histological descriptions of the bone tissue were provided, the study demonstrated that the crystallographic organization of the bone mineral in giraffes was orientated along the bone axes (i.e. 001-fibre texture), like that of modern bison, elephants and the large sauropodomorph *Apatosaurus*, and is likely in response to static stresses along the long axis of the bone. Subsequently, in a study examining the bone compactness of graviportal animals, Houssaye et al. (2016) measured the bone compactness of a modern giraffe humerus and femora (using bone profiler), and they described the bones as having a thick cortex and a proportionally smaller medullary cavity, with a wider transition zone between these domains. Indeed, the only comprehensive study to date of the bone histology of modern giraffe is a recently completed masters research by Caitlin Smith at the University of Cape Town (Smith, 2020). The latter study examined 14 giraffe specimens of known sex that spanned different ontogenetic ages. Smith (2020) provided a detailed documentation of how the histology of the long bones (femur, humerus, tibia, radius and metacarpals) changed during ontogeny, and provided an assessment of histovariability in the skeleton of giraffes.

In terms of fossil giraffes, there have been no prior studies of their bone histology. The current study fills this gap by focusing on the bone histology of the Pliocene *Sivatherium hendeyi* Harris, 1976, and *Giraffa* cf. *Giraffa jumae* Harris, 1976, from Langebaanweg (LBW) in South Africa to evaluate various aspects of their growth and biology. Langebaanweg ranks as one of the richest Neogene fossil vertebrate sites in Africa and comprises of a diverse range of vertebrates (e.g. Hendey, 1981, 1989; Rabe et al., 2022; Valenciano et al., 2022; Woolley et al., 2019). The contemporaneous extinct giraffe taxa are well represented in the faunal composition of this Pliocene locality, where they have been recovered from the 'Varswater Formation' (Harris, 1976). *Sivatherium hendeyi*, is more basal than the more common African Sivathere, *S. maurusium*. *Giraffa* cf. *G. jumae* is the first giraffe known from the west coast of South Africa (Harris, 1976; Hendey, 1982; Shorrocks, 2016). The aim of the current research is to assess the long bone histology of juvenile and adult long bones of *S. hendeyi* and *Giraffa* cf. *G. jumae* to deduce information about their palaeobiology, such as their growth dynamics, skeletal maturity, lifestyle adaptations and graviportal adaptations.

2 | MATERIALS AND METHODS

2.1 | Provenance of study material

Our study material consisted of long bone elements of *S. hendeyi* and *Giraffa* cf. *G. jumae* (Figure 1) from the Langebaanweg (LBW), a Pliocene locality on the West Coast of South Africa. All the material included in this study are from the collections housed at the Iziko Museums of South Africa in Cape Town. Permission to conduct histological analyses on 20-giraffid element from LBW was obtained from the South African Heritage Resources Agency (SAHRA permit ID 3056). Since thin sectioning is considered destructive, as far as possible, only incomplete or fragmented specimens were sampled.

2.2 | Specimen description and ontogenetic status

We include nine long bones of *Giraffa* cf. *G. jumae* comprising, two juvenile femora and seven bones from adult individuals (i.e. two tibiae, three metacarpals, one metatarsal and one metapodial). For *S. hendeyi*, we studied 11 long bones comprising two juvenile metatarsals and nine adult limb bones (i.e. one femur, two tibias, three metacarpals, one metatarsal and two metapodial). Table 1 presents a detailed list of the material examined in this study.

Notice that since our sample consists of fossil bones, we can only reliably use the anatomical features (such as unfused epiphysis) to assign ontogenetic status and we use the term 'juvenile' for an element that clearly has unfused distal/proximal ends, and 'adult' when the latter are fused. In our sample, juvenile femora of *Giraffa* cf. *G. jumae* (SAM-PQL-1252) has an unfused/ossified articulation in the proximal end. Adult *Giraffa* cf. *G. jumae* tibia sampled are fragmentary. SAM-PQL-20866 lacks the distal part (Figure 1c) but shows a fused articulation area at the proximal end. SAM-PQL-70149 does not preserve distal and proximal regions (Figure 1d). Adult *Giraffa* cf. *G. jumae* metacarpal (SAM-PQL-7408, SAM-PQL-9270, SAM-PQL-20895) and metatarsal (SAM-PQL-1274, SAM-PQL-7260) sampled are all fragmentary, preserving only the midshaft region (Figure 1e–i). Two of the metapodials (metacarpal SAM-PQL-20859a and metatarsal SAM-PQL-7260) preserved the proximal epiphysis, whereas metacarpal SAM-PQL-20859a and metatarsal SAM-PQL-7260, preserved the entire midshaft. The rest of the samples preserved only the proximal regions (SAM-PQL-7408, SAM-PQL-7260 and SAM-PQL-1274).

An adult femur of *S. hendeyi* that was studied lacked its distal epiphysis, but although the proximal region has a somewhat fragmentary cortex the proximal epiphysis is fused (Figure 1j, SAM-PQL-14266). The midshaft cross section is generally elliptical in shape (with the larger diameter in the cranio-caudal plane) with a large medullary. Adult *S. hendeyi* tibias sampled are fragmentary.

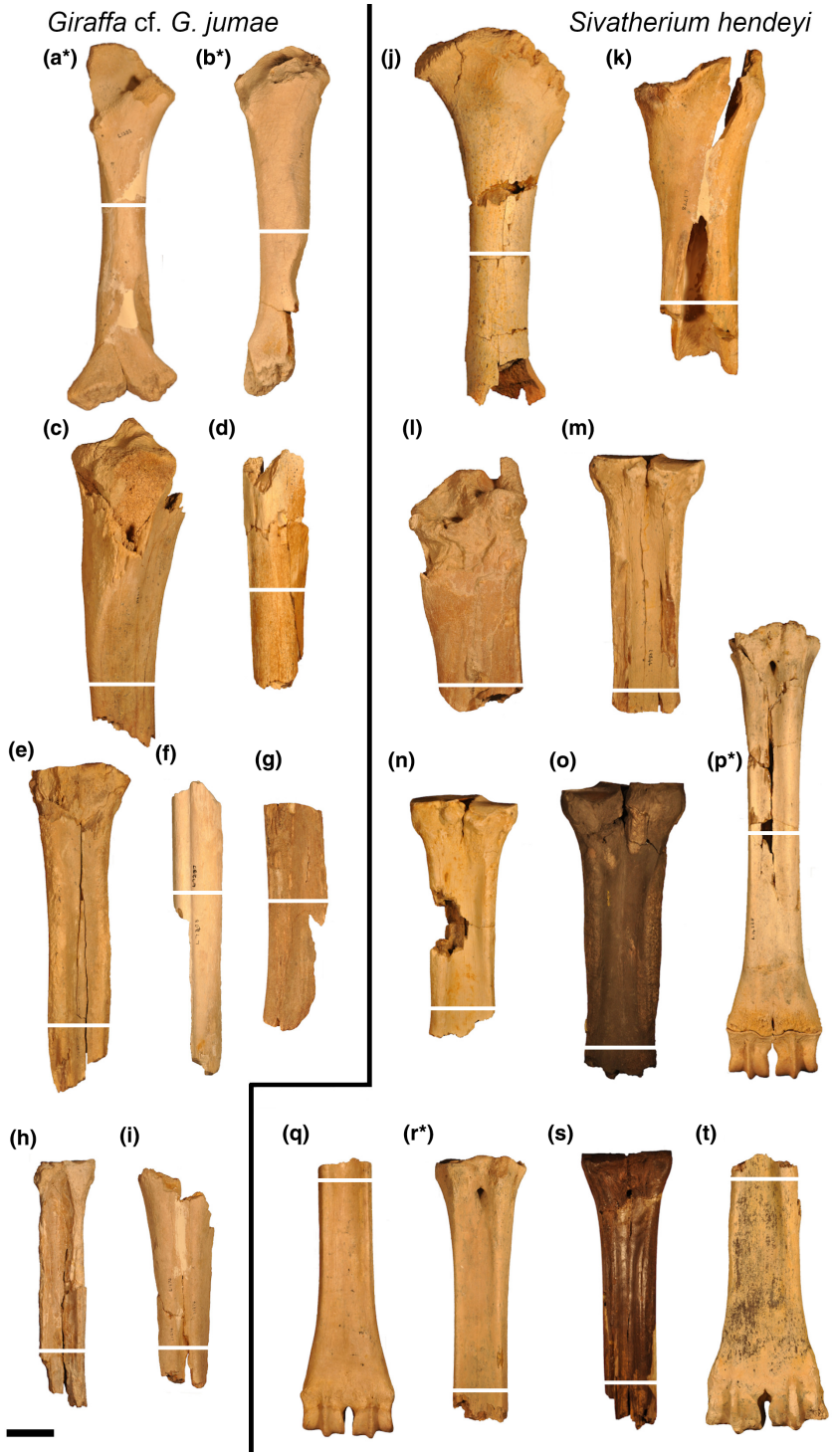

FIGURE 1 South African Langebaanweg giraffids elements sampled. (a–i) *Giraffa* cf. *Giraffa jumae*. (a, b) Femur plantar view (a, SAM-PQL-1252, b, SAM-PQL-1266). c–i, Specimens. (c, d) Tibia (c, SAM-PQL-20866 plantar view, d, SAM-PQL-70149 lateral view). (e–g) Metacarpal palmar view (e, SAM-PQL-20859a, f, SAM-PQL-7408 and g, SAM-PQL-9270). (h) Metatarsal. SAM-PQL-7260 lateral view. (i) Metapodials SAM-PQL-1274 plantar view. (j–t) *Sivatherium hendeyi*. (j) Femur anterior view SAM-PQL-14226. (k, l) Tibia plantar view (k, SAM-PQL-1778, l, SAM-PQL-4735). (m–o) Metacarpal palmar view (m, SAM-PQL-9844, n, SAM-PQL-7263, o, SAM-PQL-22523a). (p–r) Metatarsal plantar view (p, SAM-PQL-14228, q, SAM-PQL-5401, r, PQL-14145). (s, t) Metapodials palmar/plantar view (s, SAM-PQL-21562, t, SAM-PQL-45177). All the materials are adult except for the four juveniles marked with an asterisk (a, b, p and r). Scale bar, 5 cm. Transverse white line shows where the bones were sectioned.

TABLE 1 List of giraffids' long bone elements used from the Varswater Formation (Harris, 1976) Pliocene site on Langebaanweg, West Coast, South Africa

Species	Stage	Element	Collection number	Total length (cm)	Maximum diam. (cm)
Giraffa cf. *Giraffa jumae*	Juvenile	Femur	SAM-PQL-1252	36	4.52
	Juvenile	Femur	SAM-PQL-1266	37	5.26
	Adult	Tibia	SAM-PQL-20866	34	6.91
	Adult	Tibia	SAM-PQL-70149	24.6	7.64
	Adult	Metacarpal	SAM-PQL-7408	31.8	—
	Adult	Metacarpal	SAM-PQL-20859	34	6.47
	Adult	Metacarpal	SAM-PQL-9270	21.2	6.07
	Adult	Metatarsal	SAM-PQL-7260	26	4.38
	Adult	Metapodial	SAM-PQL-1274	22.7	5.55
Sivatherium hendeyi	Juvenile	Metatarsal	SAM-PQL-14145	27	5.47
	Juvenile	Metatarsal	SAM-PQL-14228	45	5.07
	Adult	Femur	SAM-PQL-14226	37.5	6.23
	Adult	Tibia	SAM-PQL-1778	33	7.81
	Adult	Tibia	SAM-PQL-4735	25.2	8.6
	Adult	Metacarpal	SAM-PQL-22523a	31.5	7.06
	Adult	Metacarpal	SAM-PQL-7263	24.5	6.62
	Adult	Metacarpal	SAM-PQL-9844	26.3	6.77
	Adult	Metatarsal	SAM-PQL-5401	28.9	5.32
	Adult	Metapodial	SAM-PQL-45177	28.5	7.13
	Adult	Metapodial	SAM-PQL-21562	27	5.37

SAM-PQL-4735 is missing the distal epiphysis, although it has a fused ossified proximal articulation. Specimen SAM-PQL-1778 is a proximal fragment, but it does not preserve the complete proximal nor distal end. Juvenile metatarsal (Figure 1p, SAM-PQL-14228) is almost complete. Specimen SAM-PQL-14145 is a more fragmentary juvenile metapodial lacking the distal region and has a total length of 270 mm (SAM-PQL-14145). Of the six adult metapodials studied, four were missing the distal epiphysis (Figure 1m, SAM-PQL-9844, N, SAM-PQL-7263, O, SAM-PQL-22523a, S, SAM-PQL-21562), while two were missing the proximal ends (Figure 1q, SAM-PQL5401, T, SAM-PQL-45177).

The anatomy of the bones was studied, and standard measurements were taken using digital callipers (Quiralte, 2011; Rios et al., 2016). All bones were photographed prior to sampling for thin sectioning.

2.3 | Osteohistology methods and terminology

For histological analyses we utilized mid-shaft sections of the limb bones or the most complete section closest to the mid-shaft since this region is considered to provide the best record of growth of long bones (Chinsamy-Turan, 2005). Standard histological procedures were used to obtain the samples of these sections (Cerda et al., 2020; Chinsamy & Raath, 1992). Histological sections were prepared by the first author (J.M.J.) in the Department of Biological Sciences at the University of Cape Town. Samples were embedded in clear resin consisting of Epoxacast resin and Epoxacast hardener (100:30) and left to harden overnight. The block was then cut with a diamond-edged saw (Abrasive cutter Impetech C10) to fit a petrographic slide (55 × 75 mm, ~1 mm thickness). The block was polished on the exposed surface using a series of abrasive carbide grinding discs (400p, 600p, 800p and 1200p) with an IMP Imptech polishing machine. The final polishing was done using Struers OP-U suspension solution on a velvet cloth covered lap-wheel. At this point, the exposed surface was flat, polished and without any irregularities. The polished surface was then mounted onto a frosted petrographic slide using Epoxacast resin and Epoxacast hardener. The specimens were mounted onto the slides were then sectioned using a precision cut-off machine (Struers Accutom). Thin sections of 120–300 μm were obtained. As Smith (2020) had found, to prevent cracking of the slides, it was best to leave the cut-off thin sections overnight to dry completely before they were ground down with the graded carbide grinding discs. Sections were checked frequently under the microscope until optimal thickness was obtained (50–30 μm). High-quality photomicrographs were taken using normal, and polarized light using a Nikon Eclipse E200 polarizing microscope and a Zeiss AX10.

For each specimen, we described the different bone tissue types following the classification of Francillon-Vieillot et al. (1990), de Margerie et al. (2002) and Chinsamy-Turan (2005). Different types of bone tissues are found in mammals: when osteogenesis

is rapid, fibrolamellar bone tissue (FLB) results (e.g. Chinsamy & Warburton, 2021; Chinsamy-Turan, 2005, 2012; de Margerie et al., 2004; Kolb, Scheyer, Veitschegger, et al., 2015) and it is characterized by a woven bone matrix wherein the fibrillar organization is disorganized (Chinsamy-Turan, 2005, 2012; de Margerie et al., 2002; Francillon-Vieillot et al., 1990). FLB is the main primary bone tissue in large mammals (e.g. Chinsamy-Turan, 2005; Currey, 2002). FLB tissue can be classified into three types based on the arrangement of the vascular channels: Laminar bone tissue (the blood vessels are organized in concentric layers around the cortex), plexiform bone tissue (the blood vessel are organized in concentric and radial connection occurs between vascular canals) and reticular bone tissue (the connection have random orientation) (e.g. Chinsamy-Turan, 2005; Francillon-Vieillot et al., 1990; Kolb, Scheyer, Veitschegger, et al., 2015). When osteogenesis is slow the result is lamellar bone tissue (Chinsamy-Turan, 2005, 2012; Currey, 2002; Francillon-Vieillot et al., 1990). This tissue comprises of thin, successive layers of lamellae in which collagen fibres are orientated parallel to each other (Chinsamy-Turan, 2005, 2012; Reid, 1996).

There are several different types of growth marks that are present in the cortical bones of vertebrates, for example, lines of arrested growth (LAGs), annuli, rest lines, neonatal line and reversal lines (Castanet et al., 2004; Chinsamy-Turan, 2005; Klevezal, 1996; Köhler et al., 2012; Kolb, Scheyer, Lister, et al., 2015; Kolb, Scheyer, Veitschegger, et al., 2015; Nacarino-Meneses & Köhler, 2018). LAGs are hyper-mineralized lines that indicate an arrest in growth (Castanet et al., 2004; Chinsamy-Turan, 2012). They have a smooth appearance that follows the contour of the external surface of the bone. The periodic arrest of bone deposition results in LAGs in the bone cortex which results in a stratification of the cortex (Castanet et al., 2004; Chinsamy-Turan, 2005, 2012; Klevezal, 1996). As a result, LAGs are often used for age determination or skeletochronological studies (e.g. Castanet et al., 2004; Chinsamy-Turan, 2005, 2012; Nacarino-Meneses & Chinsamy, 2021; Nacarino-Meneses et al., 2016b). Rest lines are grouped close together near the peripheral margin of the bone wall and are formed when appositional growth (the increase in bone diameter) has almost stopped (Castanet, 2006; Chinsamy, 1990; Chinsamy-Turan, 2012; Klevezal, 1996). They are smooth and are generally formed on unreabsorbed bone surfaces. Rest lines are often located in the OCL of mammal and bird bones and suggests slow accretionary growth once maximum body size is reached (Castanet et al., 2004; Chinsamy, 1990; Chinsamy-Turan, 2005, 2012; Klevezal, 1996; Ponton et al., 2004; Reid, 1996). Annuli are narrower than zones and they correspond to periods of slow growth. Osteocyte lacunae within annuli tend to be flattened elliptically, with poor canalicular development, which may sometimes be absent (Francillon-Vieillot et al., 1990; Montoya-Sanhueza et al., 2020). Reversal lines/tide lines are found on resorbed bone surfaces, and as the name suggests they are associated with bone remodelling or reversals in bone deposition, and as a result, the lines have a wavy appearance (e.g. Chinsamy-Turan, 2005, 2012; Klevezal, 1996). To estimate the different life history traits from the bone histology of the individuals studied here, growth marks (both annuli and LAGs) were traced along the cortex of each individual.

According to Castanet et al. (2004), cortical bone with low vascularization or low remodelling is best for recording cyclical growth marks, and for their use in skeletochronology. However, growth marks have been identified in well-vascularized mammalian bone tissue (e.g. Chinsamy & Warburton, 2021; Jordana et al., 2016; Köhler & Moyà-Solà, 2009; Nacarino-Meneses et al., 2016a). Studies of various vertebrates show that in bones in the skeleton variably record the growth dynamics of the taxon. For example, in horses the femur is best for growth mark preservation (Nacarino-Meneses et al., 2016b), whereas among deer, the humerus, femur, and tibia all maintain a good record of growth marks (Kolb, Scheyer, Lister, et al., 2015). However, in the mouse lemur (Castanet et al., 2004) and the angulate tortoise (Bhat et al., 2019) the tibia was found to be the best element for skeletochronology. In her study of the long bones of the modern giraffe, Smith (2020) found that the femora and humeri preserved the best record of growth. In the current study, although we were unable to obtain any humeri for histology study, we were able to section two femora of *G. jumae* and one of *S. hendeyi*, and we included other elements to assess the variability in the different elements.

2.4 | Abbreviations

Cr, cranial; CB, cancellous bone; ELB, endosteal lamellar bone; FO, flat lacunae osteocyte; FLB, fibrolamellar bone tissue; LAGs, lines of arrested growth; M, medial; MC, medullary cavity; Ma, million years ago; OCL, outer circumferential layer; RL, reversal line; RO, round lacunae osteocyte; ShF, Sharpey's fibre; SO, secondary osteon; WFB, woven-fibered bone.

Institutional abbreviations: SAM-PQL Quaternary Palaeontology (Langebaanweg), Iziko South African Museum, Cape Town, South Africa.

3 | RESULTS

3.1 | Osteohistology of *Giraffa* cf. *G. Jumae*

3.1.1 | Juvenile femur

The midshaft cross section of the femora of the two juveniles studied are round (SAM-PQL-1252, Figure 2a) to elliptical in shape (SAM-PQL-1266, Figure 2b). The average cortical wall thickness is between ~6 and 12 mm. Specimen SAM-PQL-1252 shows extensive bone resorption in the perimedullary region of the bone wall forming large cancellous spaces. Some remnants of the original primary bone tissue extend into the medullary cavity as trabeculae (Figure 2c–e), and some are lined with lamellar bone tissue, with round lacunae that are cut transversally, and flat lacunae in those cut longitudinally (Figure 2f, black arrow). The cortex of both juvenile femora is

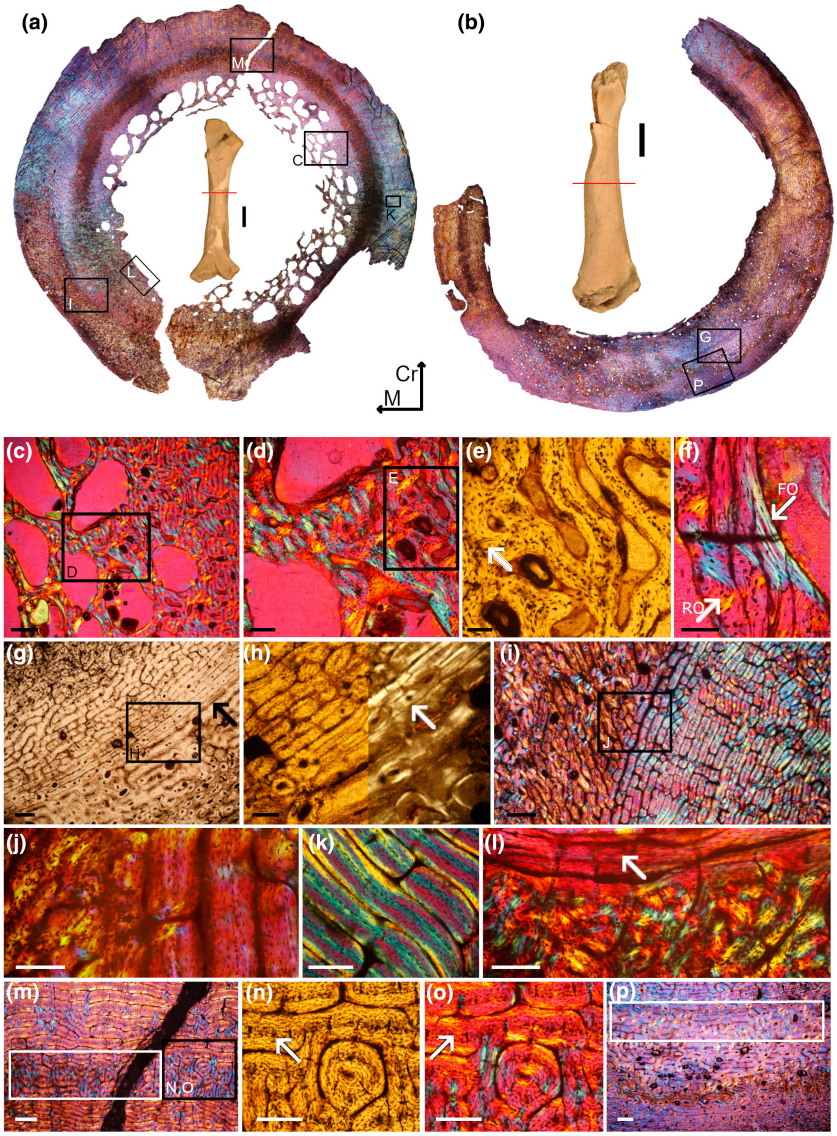

FIGURE 2 *Giraffa* cf. *Giraffa jumae* juvenile femur bone histology. (a) Specimen SAM-PQL-1252 complete cross section, viewed in polarized light with lambda filter. (b) Specimen SAM-PQL-1266 complete cross section, viewed in polarized light with lambda filter. (c–f) Detailed cancellous perimedullary bone tissue. (e) Detail Sharpey's fibres, white arrow, viewed in normal transmitted light. (f) Detail lamellar bone in the white arrow. (c,d,f) Viewed in polarized light with lambda filter. (g, h) Detailed medial cortex specimen SAM-PQL-1266. (g) Viewed in normal transmitted light with black arrow showing a LAG. (h) Higher magnification of region indicated in (g) with white arrow showing a LAG. Right half of the image is under normal transmitted light, while the left half is viewed under polarized light. (i,j) Higher magnification of the black framed region in (a) (SAM-PQL-1252) showing FLB tissue, viewed in polarized light with lambda filter. (j) Higher magnification of the black framed region in (i) showing the change of direction of the tissue, viewed in polarized light with lambda filter. (k) Higher magnification view of the mid-cortex of SAM-PQL-1252, showing laminar FLB tissue, viewed in polarized light with lambda filter. (l) Higher magnification of the framed region in (a), showing detail of ELB deposited centripetally surrounding the medullar cavity in SAM-PQL-1252, the white arrow shows fusiform lacunae, viewed in polarized light with lambda filter. (m–o) SAM-PQL 1252. (p) SAM-PQL-1266. (m–p) Middle cortex detail showing a change in tissue in the white frame. (n,o) Close detail view of the black framed region in (m), showing detail of Sharpey's fibres, black arrows. (n–p) Viewed in polarized light with lambda filter. (n) In normal transmitted light. Scale bar in (c), (g), (i), (m), (p), equals 200 μm in (d), (h), (k), (l), (n), (o) and equals 100 μm in (e), (f), (j).

predominantly formed by FLB tissue. Two regions of FLB tissue separated by a LAG are distinguishable in SAM-PQL-1266 (Figure 2g), one inner region with highly vascularized FLB and an outer region comprising of more compacted FLB (Figure 2h). The FLB tissue surrounding the medullary cavity is well vascularized with larger, more rounded osteocyte lacunae (Figure 2e), which contrasts with the exterior region that is less vascularized and the lacunae are more disc shape (Figure 2i–k). Localized variation in the histology is also visible in the medial–caudal regions of the bone wall (Figure 2j) where in higher magnification the bone tissue in the peripheral region consists of more reticular bone tissue, while the bone tissue underlying this is a mixture of laminar and reticular FLB (Figure 2j). Both femora

have a few areas where lamellar bone tissue with fusiform lacunae is deposited centripetally around the medullary cavity and form an incipient ICL (Figure 2l). The peripheral regions in the medial–caudal side comprises of laminar FLB tissue. Short Sharpey's fibres appear in most of the cortex as short plumes parallel to one another, and approximately perpendicular to the lamella of FLB (Figure 2m–o). Curiously, a distinct band of reticular FLB, like that described above, occurs in the middle cortex of the specimen SAM-PQL-1266 between layers of laminar FLB tissue (Figure 2m–o). A similar band of reticular tissue is present but not as distinct in the specimen SAM-PQL-1252 (Figure 2p).

3.1.2 | Adult tibia

The midshaft cross section of both tibiae tend to be oval, and wider along the medial–lateral plane. The average bone wall thickness is between ~10 and 18 mm, which encloses a vacant medullary cavity. Neither of the tibial cross sections have cancellous bone in the perimedullary region, although SAM-PQL-70149 appears to have more secondary reconstruction in the perimedullary region as compared to SAM-PQL-20866. Almost all parts of the medullary cavity are lined by a narrow layer of lamellar bone (Figure 3c,d), although some parts of the perimedullary region are broken (Figure 3a). A large vascular canal is visible in the medial part of the specimen SAM-PQL-70149, lined by lamellar bone (Figure 3e). The proximal part of the bone wall medullary cavity is composed by primary and secondary bone tissue, with longitudinal SO and PO (Figure 3f). The medial–caudal region of SAM-PQL-20866 has much more reticular fibrolamellar with some radially oriented vascular canals (Figure 3g,h). The medial and peripheral part of the caudal region of the cross section is composed predominately of laminar FLB (Figure 3i,j). In the specimen SAM-PQL-20866 there are five narrow annuli visible from the medial to the peripheral parts of the cross section, and these are more distinctive in the caudal lateral sector. These annuli are closer to one another in the caudal and cranial region and separated from each other in the medial and lateral region (Figure 3k,l). On the other hand, the specimen SAM-PQL-70149 has three LAGs in the medial cortex part of the caudal region and four more LAGs in the external cortex part of the lateral region (Figure 3l,m), one of which is a double LAG (Figure 3n,o). Also, SAM-PQL-70149 presents five LAGs in the perimedullary ELB. None of these lines seems to be resorption lines. The cortical bone tissue on the lateral side has undergone extensive bone remodelling (Figure 3c) and many secondary osteons are present in the cortex (Figure 3e,o).

3.1.3 | Adult metacarpal/metatarsal

Overall, the bone walls of the cross section of the metacarpal SAM-PQL-9270 (Figure 4a) and SAM-PQL-20895a (Figure 4b) are irregularly thick with the thickest part of the compact bone in the cranial region (~19 to 21 mm), while the thinnest part of the bone wall is caudally (~7 to 10 mm). None of the five metacarpals studied present cancellous bone tissue in the medullary cavity. The perimedullary margin is uneven in most of the samples (i.e. the proportion of ELB varies in different areas of the cortex) (SAM-PQL-9270 Figure 4a,c, SAM-PQL-20859a Figure 4b, SAM-PQL-1274). This margin is thicker in the cranial region of SAM-PQL-1274 (Figure 4d), and SAM-PQL-1274, thicker in the cranial and lateral region on SAM-PQL-20859a, and thinner in the cranial region in SAM-PQL-7408 (Figure 4e), and SAM-PQL-7260 and thin in the caudal region of SAM-PQL-20859a. The perimedullary margin consists of an ELB tissue forming a ICL (Figure 4c–e) with LAGs in the thicker regions of at least three samples: three LAGs in SAM-PQL-7408 (Figure 4e), five LAGs in SAM-PQL-9270 (Figure 4f) and four LAGs in SAM-PQL-20859a. Specimen SAM-PQL-9270 presents a RL between the ELB and the middle cortex (Figure 4g). Some radial canals occur in the ELB and appears to be associated with the SO of the overlying tissue (Figure 4d,f,g). Some large vascular spaces are scattered in perimedullary region of the cranial and lateral part of the cortex of SAM-PQL-9270 (Figure 4a,c). The inner cortical region of most of the samples (SAM-PQL-9270, SAM-PQL-20859a, SAM-PQL-1274, SAM-PQL-7260) is completely remodelled by SO of different sizes from large ones in the inner to smaller ones in the outer region (i.e. SAM-PQL-9270 Figure 4c). The cortex is different in specimen SAM-PQL-7408 since here predominantly primary FLB overlies the ELB perimedullary tissue and there are several longitudinally oriented SO (Figure 4e). In the SAM-PQL-20859a and SAM-PQL-7260 all the middle and outer cortex is composed of highly remodelled secondary tissue (Figure 4h). The predominant cortical bone tissue in the other specimens (SAM-PQL-9270, SAM-PQL-1274, SAM-PQL-7408) is reticular FLB (Figure 4i,j). Short Sharpey's fibres appear only in specimens SAM-PQL-9270 and SAM-PQL-1274, and only in the cranial outer region of the cortex of SAM-PQL-9270 and in the middle region of SAM-PQL-1274. The Sharpey's fibres are all radially oriented, parallel to one another and sparsely grouped in the reticular FLB tissue (Figure 4k,l). In the SAM-PQL-9270 specimen one double LAG and seven LAGs are present in the peripheral cortex (Figure 4k,l). In the peripheral cortex of SAM-PQL-1274 there are five LAGS, while in the same region of SAM-PQL-7408 there is only one LAG present (Figure 4n). Lastly, specimen SAM-PQL-9270 shows, a distinct association of vascular canals in the ELB directly associated with SO in the preceding tissue (Figure 4g,o,p,q,r).

3.2 | Osteohistology of *S. hendeyi*

3.2.1 | Adult femur

The average cortical wall thickness is between ~8 and 16 mm with the thinnest region in the cranial parts (Figure 5a). The medullary cavity is void of cancellous bone tissue and is lined with a thin layer of ELB bone tissue in the medial–lateral and caudal parts (Figure 5a) of the compacta. The inner regions of the cranial and lateral sides

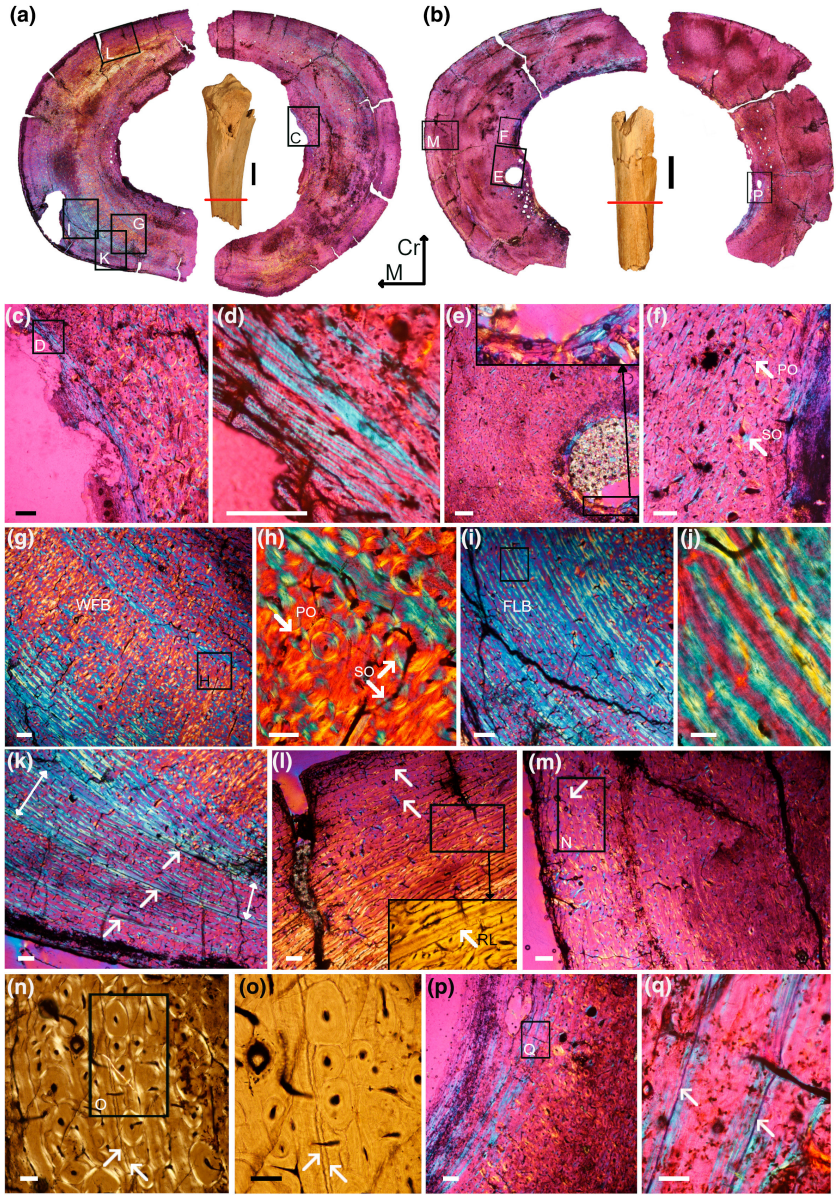

FIGURE 3 *Giraffa* cf. *Giraffa jumae* adult tibia bone histology. (a,b) Overall view of the cross sections viewed under polarized light with lambda filter. (a) Specimen SAM-PQL-20866. (b) Specimen SAM-PQL-70149. (c,d) Higher magnification of the black framed region in (a), showing the proximal part of the medullary cavity and detail of the internal cortex, polarized light with lambda filter. (e) Higher magnification of the black framed region in (b), showing the detail of the perimedullary region of SAM-PQL-70149, polarized light with lambda filter. (f) Higher magnification of the framed region in (b) showing SO and PO viewed in polarized light with lambda filter. (g) The change of direction of the bone tissue, with (h) black frame, (h) providing a higher magnification view showing PO and SO in white arrow and Reabsorption line in black arrow, polarized light with lambda filter. (i) View from the peripheral region to the mid-cortex of (a), showing the laminar FLB tissue in polarized light with lambda filter. (j) A higher magnification of the black framed region in (i), polarized light with lambda filter. (k) Higher magnification of the framed region in (a) showing the distance between LAGs, white arrow and a double LAG in black arrow, in SAM-PQL-20866, polarized light with lambda filter. (l) Showing detail of LAG white arrow and double LAG in SAM-PQL-20866. (m, n) External peripheral cortex of the medial region in SAM-PQL-70149. (m) One LAG in white arrow viewed under polarized light with lambda filter. (n) Two LAG's in white arrow with polarized filter. (o) Black frame in (n) showing detail of double LAGs, white arrow, normal transmitted light. (p) Higher magnification of the framed region in (b) internal perimedullar region in polarized light with lambda filter. (q) Higher magnification of the framed region in (p) showing two LAGs in the perimedullary cortex white arrow, in SAM-PQL-70149 view in polarized light with lambda filter. Scale bar in (c), (e), (f), (g), (i), (k), (l), (m), (p) equals 500 μm, in (d), (h) equals 200 μm and in (j), (n), (o), (q) equals 100 μm.

are composed of a laminar FLB tissue (Figure 5a,b). The ELB tissue has two distinct patterns of deposition as seen in the cross section with the lamellae crossed in two directions: one cut longitudinally with more rounded osteocyte lacunae and other transversally and therefore having a more fusiform shaped lacuna (Figure 5c–f). This laminar FLB tissue changes to a more woven fibred bone in the peripheral caudal and medial regions and shows a large amount of secondary reconstruction with secondary osteons oriented

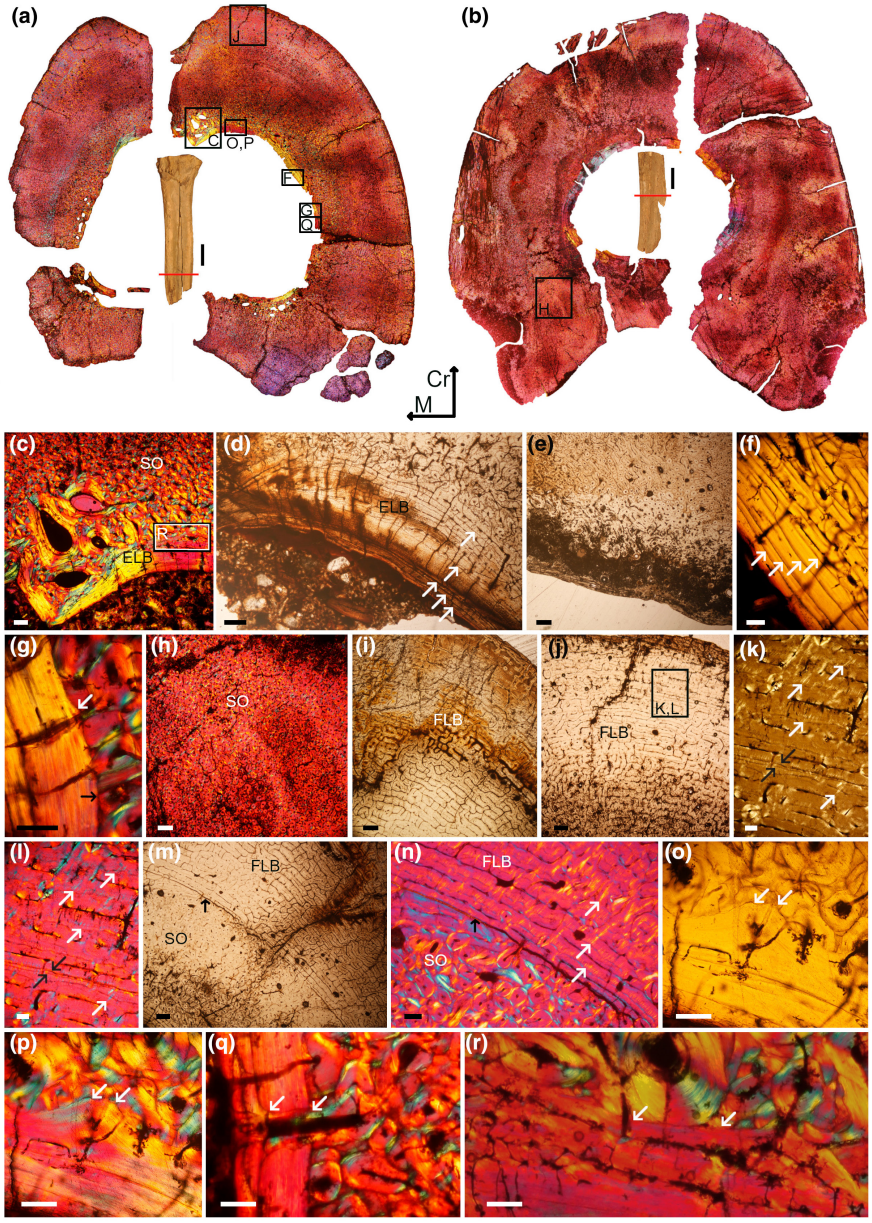

FIGURE 4 *Giraffa* cf. *Giraffa jumae* adult metatarsal and metacarpal bone histology. (a, b) Complete cross section viewed in polarized light with lambda filter. (a) Specimen SAM-PQL-9270. (b) Specimen SAM-PQL-20859a. (c) Close view of the black framed region in (a) showing the ELB tissue lining the medullary cavity, polarized light with lambda filter. (d) Close view the endosteal ELB margin is thicker in the cranial region, LAG's white arrow of SAM-PQL-1274, normal transmitted light. (e) Detail of narrow ELB in the cranial region of SAM-PQL-7408, normal transmitted light. (f) Higher magnification of the framed region in (A), showing ELB tissue with LAGs white arrows, normal transmitted light. (g) Higher magnification of the framed region in A showing a RL black arrow, between the ELB and the cortex, and radial vascular canals white arrow in SAM-PQL-9270, polarized light with lambda filter. (h) Higher magnification view of secondary tissue in the mid-cortex of the caudal medial region of SAM-PQL-20859a under polarized light with lambda filter. I, close view of peripheral cortex in SAM-PQL-1274 showing reticular FLB, normal polarized light. (j–l) Close view of external cortex FLB of SAM-PQL-9270, showing Sharpe's fibres in white arrows and double LAG in black arrow, (j) higher magnification of the framed region in (a) under normal transmitted light, (k) viewed under polarized light, and (l) viewed under polarized light with lambda filter. (m, n) Detail of mid-cortex of the cranial region of SAM-PQL-1274 showing the change of tissue from a highly remodelled tissue with SOs to FLB. A RL is indicated by the black arrow and Sharpey's fibres by the white arrow, (m) under normal transmitted light, (n) viewed under polarized light with lambda filter. (o–r) Perimedullary region showing the ELB tissue, associated with vascular canals, and overlain by secondary tissue with numerous SO white arrow. (o) normal transmitted light, (p–r) polarized light with lambda filter. (q–r) are higher magnification of the regions. Scale bar in (c), (d), (e), (h), (i), (j), (m) equals 500 μm, in (f), (g), (n), (o), (p), (k), (r) equals 200 μm and in (k), (l) equals 100 μm.

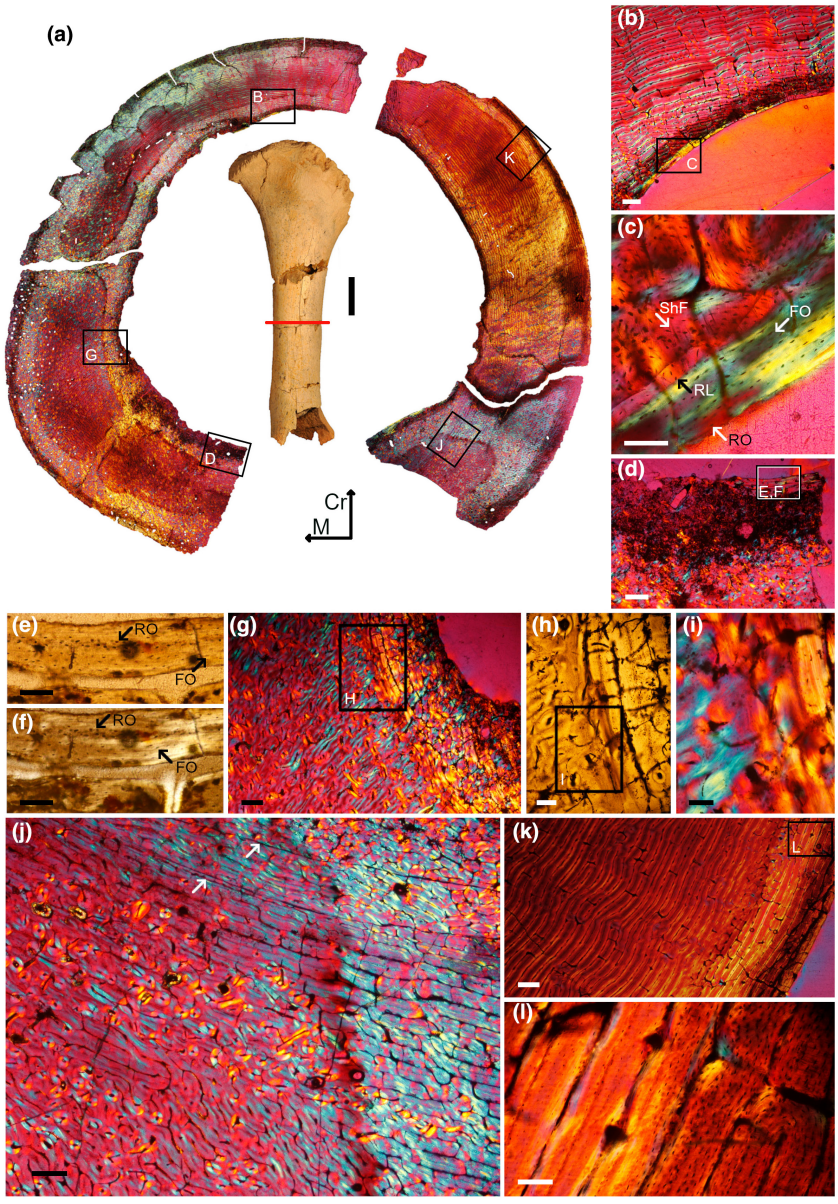

FIGURE 5 *Sivatherium hendeyi* adult femur SAM-PQL-14226 bone histology. (a) Complete cross section, viewed under polarized light with lambda filter. (b, c) Higher magnification of the perimedullary region as indicated in (a), polarized light with lambda filter. (d–f) Higher magnification views as indicated in (a), and (d) (e, f) Higher magnification views as indicated in (d) showing round lacunae (RO) and fusiform lacunae (FO) black arrow. (d) Under polarized light with lambda filter, (e) under normal transmitted light, (f) under polarized light. (g) Higher magnification view of the framed region indicated in (a), showing the perimedullary region of the caudal medial side, polarized light with lambda filter. (h) Higher magnification view of the framed region indicated in (g) showing the gradual change in the tissue and orientation of the vascularization, normal transmitted light. (i) Higher magnification view of the framed region indicated in (h) showing the histological changes under polarized light with lambda filter. (j) Higher magnification view of the framed region indicated in (a) showing secondary reconstruction, reticular FLB and LAG's white arrows, under polarized light with lambda filter. (k) Higher magnification view of the framed region indicated in (a), showing laminar FLB (l), shows detail of the framed region in (k). Scale bar in (c), (d), (g), (j), (k) equals 500 μm, in (h) equals 200 μm and in (c), (e), (f), (i), (l) equals 100 μm.

longitudinally, radially and some circumferentially (Figure 5g–j). Three to four LAGs tend to be in the peripheral parts of the cranial and medial region of the cortex, two are clear in the medial region (Figure 5j, white arrows) and the other disappear in the peripheral parts. The cortex is extensively remodelled with primary and secondary osteons present. The peripheral regions are also formed by a laminar FLB tissue (Figure 5k,l).

3.2.2 | Adult tibia

The cross section is elongated into an oval shape that is wider along on the medial–lateral plane. The average bone wall thickness is between ~14 and 22 mm, and it encloses a vacant medullary cavity. The medullary cavity is lined with lamellar bone tissue, with is interrupted by RL in the caudal part (Figure 6a,b). The reconstruction of

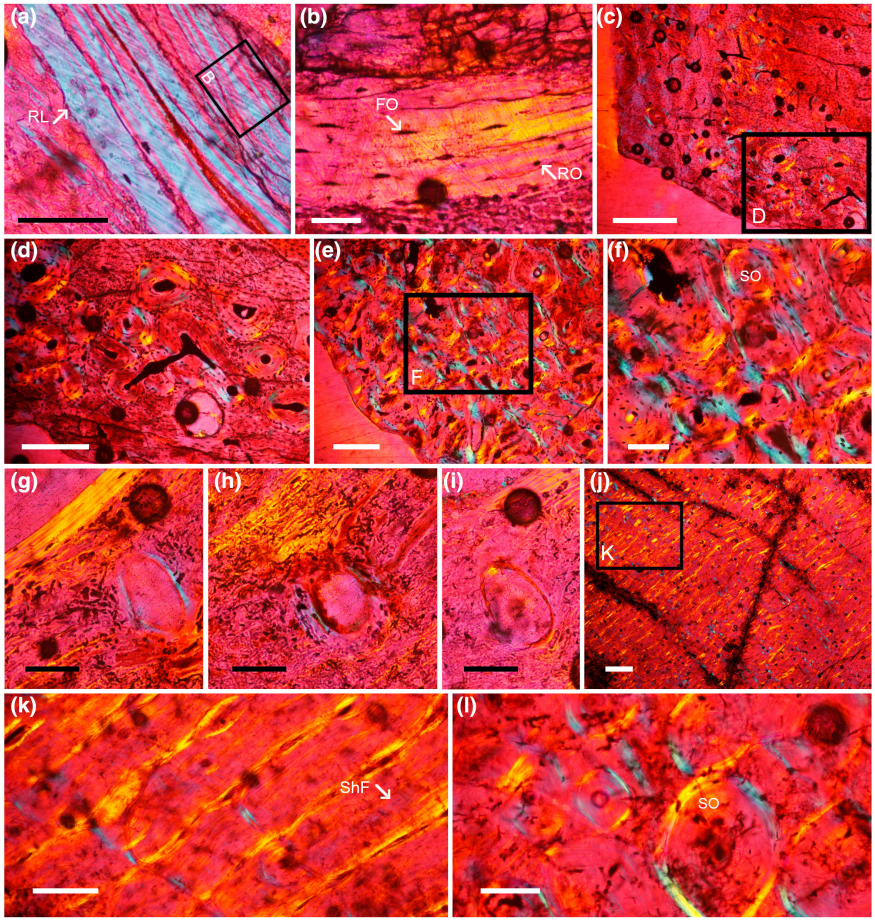

FIGURE 6 *Sivatherium hendeyi* adult tibia bone histology (PQL-1778) all images are viewed under polarized light with lambda filter. (a) High magnification showing lamellar tissue lining the medullary cavity caudal part, RL in white arrow. (b) High magnification of the internal ELB showing round lacunae osteocyte (RO) and fusiform lacunae osteocyte (FO) white arrow. (c–f) Caudal lateral part of the perimedullary cortex showing the extensive development of secondary osteons. (d) Higher magnification of the framed region in (c) showing well-formed secondary osteons and erosion cavity. (e) Caudal lateral part showing a mix of primary and secondary osteons. (f) Detail in (e) showing secondary osteon. (g–i) Detail of eroded vascular spaces lined with endosteally formed lamellar bone. (j) Detail of the peripheral part region of the cross section laminar FLB. (k) Higher magnification of the framed area in (j) showing detail of FLB and Sharpey's fibres white arrow. (l) Caudal lateral regions of the mid-cortex extensively reconstructed secondary osteons. Scale bar in (a), (b), (h), (i), (j) equal 100 μm, in (c) equal 50 μm, in (d), (f), (k) equal 500 μm, in (e), (g), (l) equal 200 μm.

the complete cross section was not possible because of the preservation of the specimen. In some regions we can distinguish each one of the laminae in the laminar bone (Figure 6a). As described previously the ELB tissue appears to be deposited in two directions as indicated by the alternating fusiform and more rounded osteocyte lacunae (Figure 6b). Some posterior medial part of the perimedullary region have secondary reconstruction right up to the edge of the medullary cavity (Figure 6c–f), while in other parts the medullary cavity is lined by an endosteal deposit of lamellar bone tissue that can be thick (Figure 6a) or thin (Figure 6g–i). Large erosional vascular spaces, often lined with endosteally formed lamellar bone, are observed frequently in the perimedullary region in SAM-PQL-1778 (Figure 6g–i). The peripheral part region of the cross section is composed predominately of laminar FLB (Figure 6j,k). Short Sharpey's fibres appear parallel one another in the FLB tissue (Figure 6k). In the caudal and lateral regions of the cross sections the cortical bone is extensively reconstructed and there are many secondary osteons present (Figure 6l).

3.2.3 | Juvenile metatarsal/metapodial

The cross sections of one of the metatarsals show that the medullary cavity is bisected by a band of primary woven bone tissue (Figure 7a, SAM-PQL-14228). Closer inspection of the bone tissues revealed that the unusual microanatomy is the result of the fusion of metacarpals III and IV. Overall, the bone wall of the cross section of the fused metacarpal is irregularly thick with the thickest part of the compact bone in the cranial region (~7–21 mm), while the thinnest bone wall is in the caudal region opposite to the thickest part (~7–10 mm). The inner region is void of cancellous bone tissue in the medullary cavity. The perimedullary margin consists of a circumferential FLB tissue

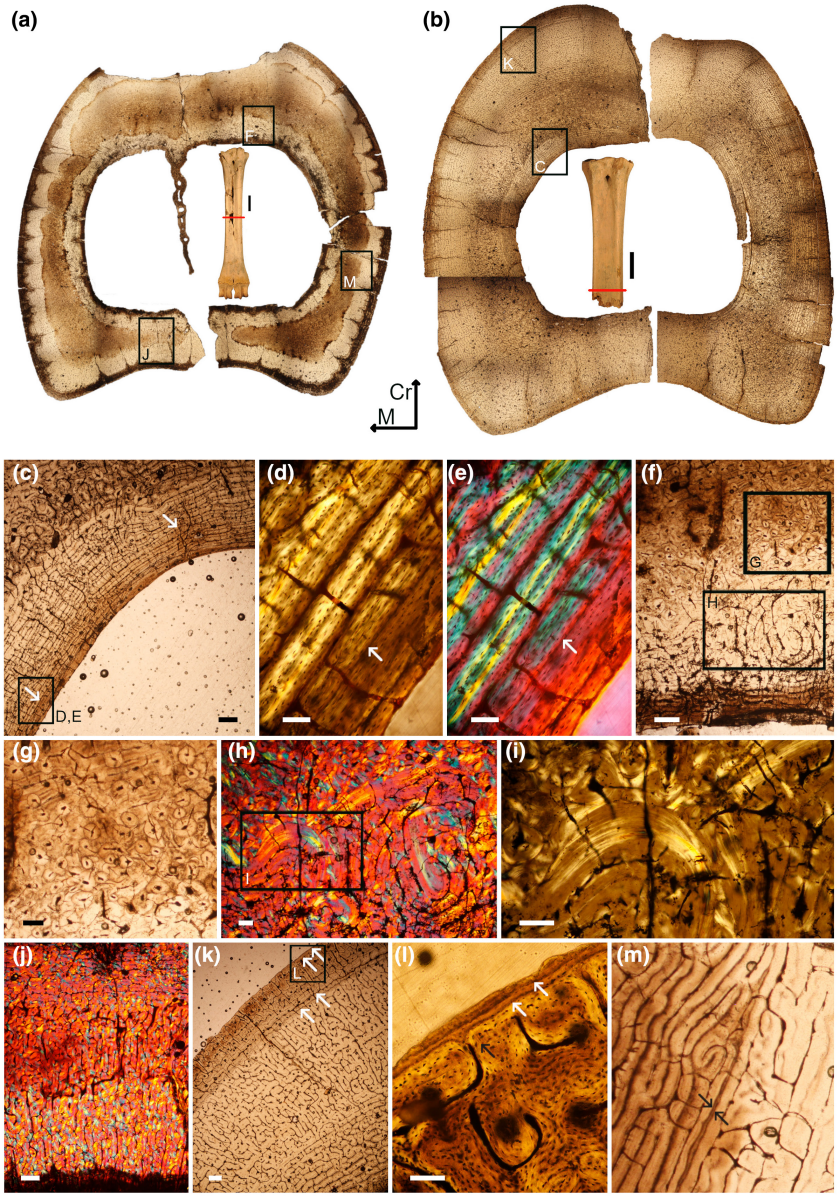

FIGURE 7 *Sivatherium hendeyi* juvenile metapodials bone histology. (a) Overview of the cross section of specimen SAM-PQL-14228. (b) Overview of the cross section of specimen SAM-PQL-14145. (c–e) Higher magnification of the medial cranial perimedullary region, under normal transmitted light in SAM-PQL-14145. (d,e) A higher magnification of the framed region in (c) showing ELB, white arrow indicates the LAG. (d) Detail of ELB in (c) under polarized light, (e) Detail of ELB in (c) under polarized light with lambda filter. (f–i) Higher magnification of the tissue in the cranial region of SAM-PQL-14228. (f–g) Detail of remodelled region with secondary osteons under transmitted normal light, (h) Detail of compact coarse cancellous bone tissue under polarized light with lambda filter, (i) close view compact coarse cancellous bone frame in (h) under polarized light. (j) Reticular and radial FLB higher magnification of the framed region in (a). (k–l) Peripherical medial cranial region of SAM-PQL-14145 showing two LAGs white arrows and Sharpey's fibres black arrow, under normal transmitted light. (l) Close view frame in (l) of Sharpey's fibre black arrows end LAG's white arrows. (m) Detail of double LAG black arrows in the external peripheral region of SAM-PQL14228, under normal transmitted light. Scale bar in (c), (f), (j), (k) equals 500 μm, in (g), (h), (i), (m) equals 200 μm and in (d), (e), (l) equals 100 μm.

with fusiform lacunae and some radial vascular canals (Figure 7c–e). Contiguous to these tissues there is highly remodelled FLB with numerous SO in the cranial, lateral and medial regions (Figure 7f,g). In the inner part of the cranial region of SAM-PQL-14228 a compact coarse cancellous bone tissue occurs (Figure 7f,h,i). In both samples in the caudal region the tissue is mainly reticular FLB with vascular canals in the outermost cortex principally oriented in a radial direction (Figure 7j). The middle part of the compacta comprises of a laminar FLB that becomes more reticular towards the external peripheral region (Figure 7k–m). There are six LAGs present in the peripheral region of SAM-PQL-14145 four of them in the peripheral region (Figure 7k,l, white arrows) and another LAG occurs in the inner FLB (Figure 7d,e). Only one, a double LAG, appears in SAM-PQL-14228 in the mid-cortex (Figure 7m). Short Sharpey's fibres

occur only in SAM-PQL-14145; these are scattered, parallel to one another and perpendicular to the external surface (Figure 7l).

3.2.4 | Adult metacarpal/metatarsal/metapodial

The cross sections of the metacarpals tend to be thick in the medial and lateral caudal regions (Figure 3a,b). The cross sections of four metacarpals (SAM-PQL-22523a, SAM-PQL-9844, SAM-PQL-7263, SAM-PQL-45177) and one metapodial (SAM-PQL-45177) are distinct in that the medullary cavity is bisected by a band of primary bone tissue (Figure 8a,b,d,e,f). At this stage the independent histology of MC III and IV is still visible. Only one of the metacarpals studied has a lot of cancellous bone tissue present in the perimedullary region (Figure 8b,d,f). The cancellous spaces are lined with lamellar bone tissue, and they tend to be compacted to form compact coarse cancellous bone tissue (Figure 8e,g). Large SO and erosional cavities occur close to this cancellous bone tissue in SAM-PQL-9844 (Figure 8i,k) while in the other samples the remodelled secondary tissue overlies the ELB tissue (Figure 8i,j). The ELB has several LAGs: eight to nine LAGs for SAM-PQL-5401, where two are a double LAG (Figure 8j white arrow) and another is a triple LAG (Figure 8j black arrow) and four LAGs for SAM-PQL-22523a. In SAM-PQL-7263 FLB tissue occurs in the lateral side close to the inner perimedullary ELB, preceding the secondary remodelled tissue. Also, in specimen SAM-PQL-5401 a narrow band of FLB occurs in between two layers of ELB tissue (Figure 8l). The cortical bone tissue is highly remodelled, with many secondary osteons present and resorption cavities on the lateral caudal regions. The middle region of the periosteal margin is reconstructed by SO which extend into the medial, lateral and cranial sides, and also into the external caudal region in most of the samples. The external cortical bone tissue is reticular or laminar FLB. Short Sharpey's fibres are parallel one another in the FLB tissue and are oriented perpendicular to the external surface in most of the samples. Long Sharpey's fibres occur in the caudal lateral and medial sector (Figure 8o). LAGs also occur in the external periphery cortex, they tend to appear singly or grouped in triplets (Figure 8p, SAM-PQL-7263, Q, SAM-PQL-9844). In metacarpal SAM-PQL-22523a (Figure 1o) and metapodial SAM-PQL-21562 (Figure 1 S, SAM-PQL) the bone matrix is carmine red to ochre orange in colour, but histological features are evident as in the other samples (Figure 9). No carbonization is seen within the pore spaces of the sections.

4 | DISCUSSION

4.1 | Fossil giraffe bone microanatomy and histology as compared to the modern giraffe

Our results show that as in the modern giraffe, *G. camelopardalis* (Smith, 2020), the fossil giraffes had similar bone wall thickness, and showed a clear distinction between the thick cortical wall and the open medullary cavity. In a previous study, van Schalkwyk et al. (2004) found that the cortical thickness of modern giraffe bones was significantly greater than those of equivalent buffalo skeletal elements. They proposed that the midshaft limb bone strength of giraffes is related partially to the greater relative cortical thicknesses as well as the relative straighter limb bones, as noted also by Biewener (1983). Additionally, van Schalkwyk et al. (2004) proposed that giraffe limb bones (and those of buffaloes) are denser than other non-limb bone elements, and they suggested that bone density contributes to bone strength. However, it should be noted that caudal cortical thickened metapodials is not a feature unique to the modern giraffe and can be found in many members of the Giraffidae, even among the much lighter okapi (Skedros et al., 2007).

As in the extant *G. camelopardalis* (Smith, 2020), the different ontogenetic stages of *Giraffa* cf. *G. jumae* presented distinctive bone histology, that is, juveniles (e.g. femur, SAM-PQL-1252) had extremely well-vascularized FLB and showed cancellous bone in the perimedullary region (Figure 8b,d,f). As the juveniles matured, the cortical bone tissue changed to a more slowly deposited bone tissue (which became less vascularized and more lamellar), with growth marks tending to occur in the outer parts of the cortex. The juvenile metatarsal of *S. hendeyi* did not show CB, presented six LAGs in the peripheral region, a LAG in the inner FLB near the perimedullary region, as well as a two closely associated LAGs which we refer to as a double LAG (and consider as likely to be caused by a single event) in the mid-cortex (Figure 7m). It is therefore apparent that despite its young ontogenetic status, this individual experienced several interruptions in its growth. Additionally, only one adult metacarpal of *S. hendeyi* (SAM-PQL-9844) showed a large amount of CB (Figure 8b,d,f) like *G. camelopardalis*. However, we are uncertain if these differences observed are intrinsic for the species since we have only examined a small sample.

In her study of the long bones of the modern giraffe, Smith (2020) found that only the tibia showed long radially organized vascular canals that straddled large parts of the compacta. Similar vascular features have been reported in the giant extinct elephant birds (aepyornithids) (Chinsamy et al., 2020) and the sauropterygian *Cymatosaurus* (Klein, 2010). In the current study, we found similar elongated radial vascular canals in the tibia, but also in the adult metacarpals of *Giraffa* cf. *G. jumae*, as well as in the juvenile metapodials of *S. hendeyi*. However, these radially organized elongated canals are sparse in the extinct giraffes as compared with their abundance in the tibia of their modern relatives.

Kolb, Scheyer, Lister, et al. (2015) found that the humerus, femur and tibia all kept a good track record of the growth of deer, whereas among *Equus* (Nacarino-Meneses et al., 2016a, 2016b), and modern giraffes (Smith, 2020) the femora appeared to be best for skeletochronology. In fact, Smith (2020) reported that both the humerus and femur of the modern giraffe (*G. camelopardalis*) maintain the highest number of growth marks in both subadults and adults, and as in the fossil giraffes we studied, these tended to be restricted in the outer part of the cortex. Of the over 64 elements studied (from 21 individuals) of *G. camelopardalis*, only 11 elements (humerus, radius, femur, tibia) exhibited growth marks (annuli) (Smith, 2020).

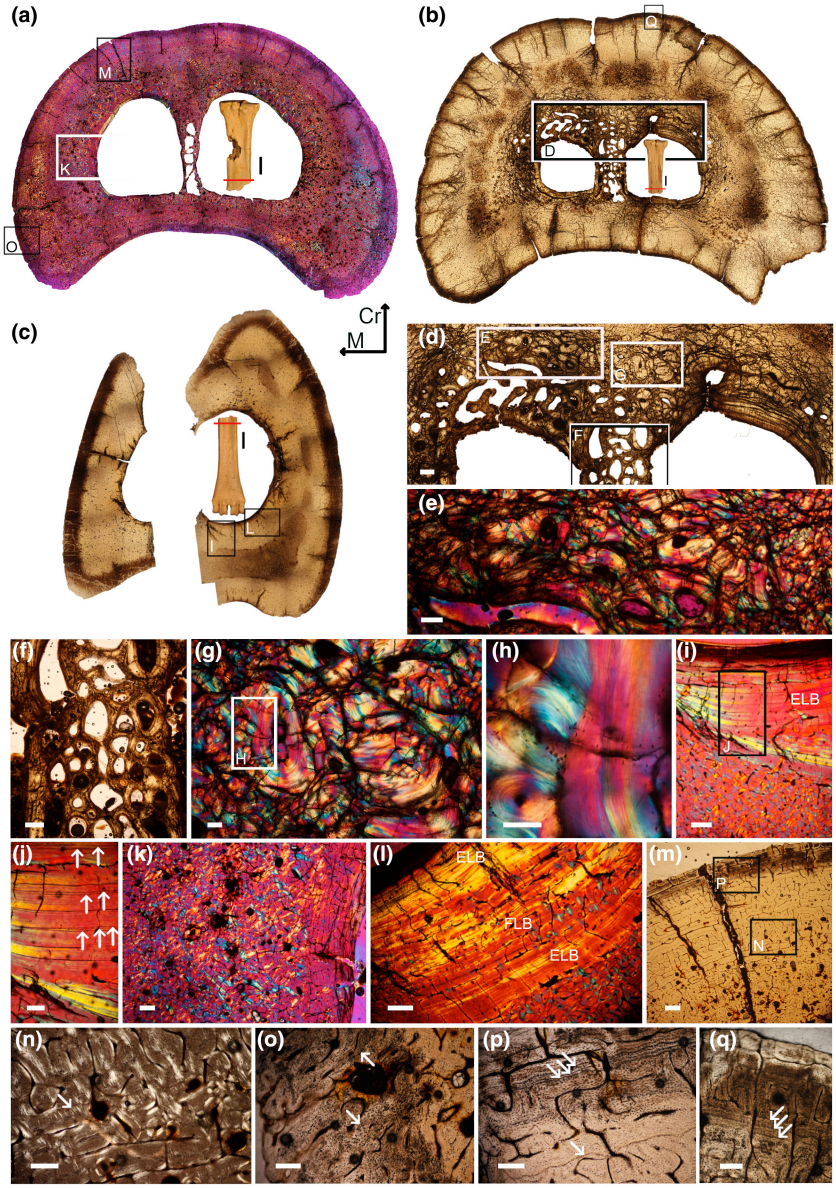

FIGURE 8 *Sivatherium hendeyi* adult metacarpal and metatarsal bone histology. (a), Overview of the cross of metacarpal SAM-PQL-7263 under polarized light with lambda filter. (b) Overview of the cross section of metacarpal SAM-PQL-9844 under normal transmitted light. (c) Overview of the metatarsal SAM-PQL-5401 under normal transmitted light. (d–h) Views of perimedullary cranial region of the medulla in SAM-PQL-9844. (e) Close view frame (d) showing coarse cancellous bone. (f) Close view frame D showing normal cancellous bone. (g, h) magnification showing the change of direction in resorption lines in lamellar bone under polarized light with lambda filter. (i,j) Magnification of the perimedullary ELB of the caudal region in SAM-PQL-5401. (j) Higher magnification of the framed region in I showing endosteal lamellar bone with detail of double LAG white arrows, and triple LAGs black arrows in metatarsal SAM-PQLc-5401. view in polarized light with lambda filter. (k), Higher magnification of the framed region in (a), showing the extensive secondary reconstruction in the perimedullary region, under polarized light with lambda filter. (l) Higher magnification of the framed region in (c) showing ELB and FLB tissues in the perimedullary, polarized light with lambda filter. (m,n) Higher magnification views of the framed region in (a) showing reticular FLB (m) under normal transmitted light, (n) detail on Sharpey's fibre white arrow, under polarized light. (o) Detail of Sharpey's fibres caudal region of metacarpal SAM-PQL 7263. (p,q) High magnification of three consecutive LAGs in external peripheral cortex cranial region of SAM-PQL-7263 (p) and SAM-PQL-9844 (q). Scale bar in (d) equal 1000 μm, in (e), (f), (i), (k), (l), (m) equals 500 μm, in (g), (j), (n), (o), (p), (q) equal 200 μm and in (h) equals 100 μm.

As in modern giraffes (Smith, 2020), we could readily identify metacarpals from early ontogenetic stages of *Giraffa* cf. *G. jumae* and *S. hendeyi* based on their histology which clearly showed the fusion of metacarpals III and IV. In addition, we found that despite the intense remodelling evident in the metatarsals several LAGs were still observable in both the fossil taxa (contra the situation in modern giraffes, Smith, 2020). Indeed, we found that bone growth marks (BGMs) were recorded in almost all bones of *Giraffa* cf. *G. jumae* and

S. hendeyi (e.g. the juvenile femur *Giraffa* cf. G. *jumae* shows a single LAG in the middle of the cortex, which separates two deposits of FLB; Figure 2g,h). In the bones of *S. hendeyi* several of the bones exhibited growth marks: juvenile metapodials had about six LAGs occurring peripherally in SAM-PQL-14145 (Figure 7k,l), as well as another LAG occurring near the perimedullary region (Figure 7d,e). In addition, in at least three adult specimens (SAM-PQL-7408; [Figure 4e white arrow], SAM-PQL-9270 [Figure 4f] and SAM-PQL-20859), an ICL with multiple rest lines interrupting the deposition of the lamellar bone tissue was found. Such pauses in the rate of endosteal formed bone tissue have been recorded in several taxa, including *G. camelopardalis* (Smith, 2020), echidna (Chinsamy & Hurum, 2006) and in cape dune mole rats (Montoya-Sanhueza & Chinsamy, 2017). The rest lines divide the ICL into bands of bone tissue (Amprino, 1947; Enlow, 1963), and indicate periodic pauses in the rate of endosteal bone deposition (Castanet et al., 2004; Chinsamy-Turan, 2005).

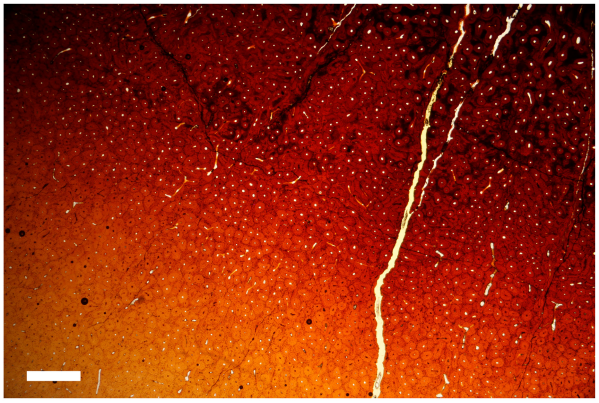

FIGURE 9 *Sivatherium hendeyi* metacarpal SAM-PQL-22523 showing the characteristic features of a burnt bone under normal light. scale bar 1 mm.

4.2 | Biological inferences of the BGMs

Inferences of longevity and age at maturity of extinct and extant vertebrates are often based on the study of BGMs by means of skeletochronology (Chinsamy & Warburton, 2021; Chinsamy-Turan, 2005; Jordana et al., 2016; Köhler & Moyà-Solà, 2009; Marín-Moratalla et al., 2013; Moncunill-Solé et al., 2016; Nacarino-Meneses et al., 2016b; Schucht et al., 2021; Woodward et al., 2013). Köhler et al. (2012) demonstrated that the annual formation of LAGs occurs among ruminants and that the cyclic arrest of growth in bone is triggered by hormonal cues rather than environmental stresses. Interestingly, physiological studies of kangaroos have shown that thermal stress during intense dry seasons in Australia result in decreased growth and activity levels (Arnold et al., 1991), which Chinsamy and Warburton (2021) correlated with growth marks in kangaroo bones. It is apparent that despite all the research on skeletochronology the precise reason for their formation is still uncertain, although it appears that they are correlated with a combination of environmental, hormonal and innate biological cues.

Assuming, that each LAG (or groups of double and triple LAGs) represents an unfavourable event (e.g. Chinsamy & Warburton, 2021; Nacarino-Meneses et al., 2016a, 2016b), we found that the different skeletal elements studied had a variable number. Surprisingly we found that in *S. hendeyi* the juvenile metacarpal recorded more growth marks as compared to the adult bones (Figure 10). It is possible that some earlier growth marks in the adults might have been resorbed. In the *G. jumae* specimens we found that the adult tibia had the greatest number of LAGs, while the juvenile femur had just one LAG (Figure 10). It should also be noted that in her study of known age modern giraffes, Smith (2020) did not find any correlation between the age of the animal and the number of LAGs in the compacta of the bones. These findings lead us to suggest that the LAGs observed in the cortex of the extinct giraffids may not necessarily

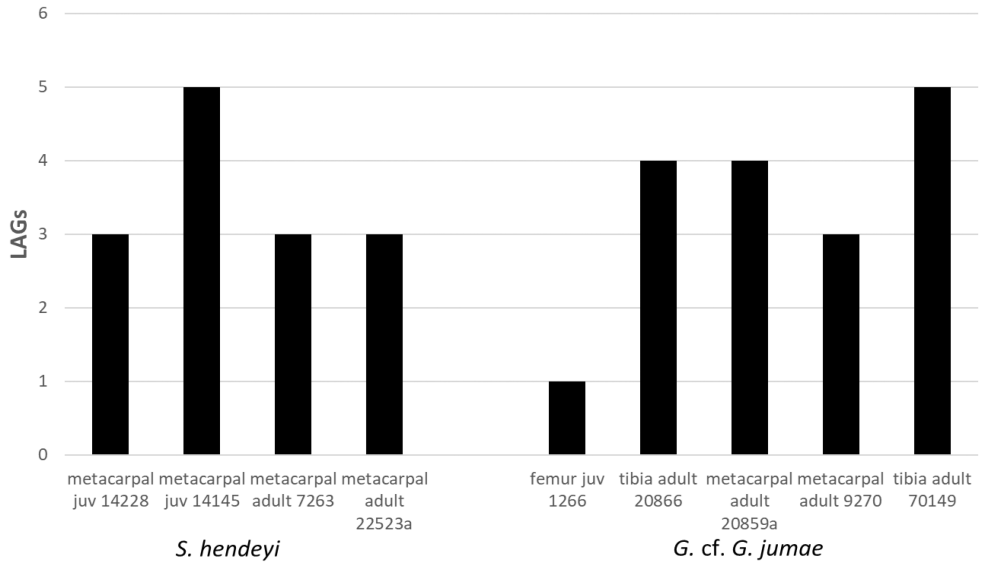

FIGURE 10 Lines of arrested growth summary observed in the medial and peripheral cortex of *Sivatherium hendeyi* and *Giraffa* cf. *Giraffa jumae*.

be annual and could likely represent periodic stressful periods. This appears to be the case for some other known aged vertebrates (e.g. Schucht et al., 2021).

Indeed, Hendey (1981) had suggested that the large numbers of herbivores in the LBW deposits were the result of changing environmental conditions of the late Miocene and early Pliocene, when local temperatures moderated from tropical to temperate, and the rainfall pattern also switched from summer to a winter maximum, consequently changing the environment from a typical woodland vegetation to more open grasslands and fynbos. Thus, it is likely that these unstable environmental conditions were stressful for the giraffids (and other herbivores) that lived at this time. Furthermore, in a study of over 2000 teeth of *Sivatherium* from LBW, Franz-Odendaal et al. (2004) found that about 34% of the deciduous teeth and 40%–75% of the permanent teeth showed enamel hypoplasia, while 20%–35% of the permanent teeth displayed linear hypoplasia. The linear defects at the base of the first molar are associated with stress caused by weaning, whereas the pathologies evident on the permanent teeth were thought to be related to episodic periods of environmental stress such as nutritional stress (Franz-Odendaal et al., 2004).

In a study of modern giraffes O'Connor et al., (2019) found that during severe drought conditions in Zimbabwe, the oldest and largest individuals (especially males) and the young juveniles in the population were at highest risk of death, while young adults seemed to have a higher survivorship. Interestingly, using dental crown heights to establish mortality profiles for the giraffids *S. hendeyi* and *Giraffa* sp., the bovids *Mesembriportax acrae* and *Simatherium demissum*, and the rhinoceros *Ceratotherium praecox* from the early Pliocene Varswater Formation, Klein (1981) suggested that the giraffid mortality profiles exhibit classic 'catastrophic' shapes, in which progressively older age classes contain progressively fewer individuals. Since the giraffid remains were recovered from what is thought to have been an ancient river channel, it is possible that they drowned or that the animals died near the water's edge during droughts and then when the rains arrived, their remains got washed into the channel. Interestingly, giraffid bones far outnumber those of other species in the channel fill, and the mortality profiles of the other species all exhibit 'attritional' shapes, in which prime-age adults are seriously under-represented relative to their probable live abundance (Klein, 1981). Thus, considering these all these findings of both fossil and modern giraffes, we propose that the deposition of LAGs in the cortex of the giraffids from LBW reflect periodic harsh environmental conditions. Thus, the six LAGs in a juvenile metacarpal show that it endured at least six stressful periods, which could but may not necessarily be annual events.

4.3 | Burnt bone

The occurrence of burnt bone in Langebaanweg deposits was recognized by Hendey (1982). Subsequently, in a study of the diagenetic changes present in the bones and teeth at LBW, Brumfitt et al. (2013) found that some bones were sub-aerially exposed before burial as evidenced by being burnt. The occurrence of burnt bone in the deposit of LBW is attributed to bushfires during seasonally dry or long-term drought periods (Brumfitt et al., 2013).

During combustion, bones exhibit varying degrees of structural and textural modifications (Hanson & Cain, 2007; Shipman et al., 1984), and the degree of shrinkage, fracturing, cracks, deformation, coloration and warping is a direct measure of the temperature at which bones were heated or burned (Brain & Sillen, 1988; Ellingham et al., 2015; Kalsbeek & Richter, 2006). Such burnt bones are the focus of many forensic, archaeological and palaeontological studies (e.g. Absolonová et al., 2012; Bhat et al., 2021; Shipman et al., 1984). Fire induces a variety of macroscopic (size, colour and shape) and chemical changes in skeletal elements (Brain & Sillen, 1988; Fairgrieve, 2008; Reidsma et al., 2016; Shipman et al., 1984; Taylor et al., 1995; Ubelaker, 2009; van Hoesel et al., 2019), therefore, their identification and characterization by visual assessments can often be misleading. Shipman et al. (1984) conducted a controlled heating experiment on modern bones and teeth of sheep and goats and documented a series of colour and surface changes as heating progressed to higher temperatures. Recently, Bhat et al. (2021) examined burnt and unburnt tibiae of angulate tortoises from the intermediate and late Howiesons Poort levels at Diepkloof Rock Shelter of Western Cape, South Africa, and deduced a suite of heat-induced osteohistological changes. They recognized three types of bone damage caused by fire: (a) external colour change in the bones but otherwise consistent osteological and histological features to unburnt bones; (b) partially burned bones with osteological features obliterated, but histological details still preserved, and carbon inclusions visible along the bone margins and within pore spaces; and (c) completely burned bones with obliterated osteological features, but overall shape is maintained, and except for the presence of cracks and carbon accumulations within pore spaces and around the periosteal margin, histological features are evident.

In the current study, a metacarpal (SAM-PQL-22523a) and an indeterminate metapodial (SAM-PQL-21562) are distinctly dark brown to almost black in colour (Figure 1, O, S, SAM-PQL-21562). Upon sectioning the bones, the bone matrix of the histological section appeared carmine red to ochre orange (Figure 9), although all the histological features were preserved. This appears to be like the first category of bones that Bhat et al. (2021) described, since no major cracks or alteration of the bone tissue were observed, and no carbon deposits within the pore spaces was observed. These findings suggest that the bones had experienced a low heat intensity of possibly less than 300°C (e.g. Bhat et al., 2021; Brain, 1993; Herrmann, 1976, 1977; Nelson, 1992) that mostly affected its coloration but did not damage the microscopic structure of the bones.

4.4 | Limitations of this study

Although the current study is novel in that it permitted insight into the biology and histology of limb bones of two extinct giraffe taxa,

it is limited in that the sample poorly represents different stages of ontogeny. Additionally, the small sample size precluded the use of statistical analysis. Thus, if more fossil giraffe specimens become available for histological study, it would be ideal to obtain a more robust sample of different ontogenetic stages to assess the validity of the findings observed in the current study. Furthermore, it would be useful if known age modern giraffes could be studied to ascertain whether the growth marks observed in their compact bone reflect their ontogenetic age or as we propose other environmental or physiological stress experienced by the animal.

5 | CONCLUSIONS

In this study we show the histological characteristics in several limb elements of fossil giraffes. The histovariability observed in the skeletons of *Giraffa* cf. *G. jumae* and *S. hendeyi* shows the general pattern observed in mammals, that is., fast rates of growth in the juveniles and slower growth rates as the animals mature, as well as the development of extensive secondary reconstruction in the cortex with age. We postulate that the growth marks (LAG) observed in the giraffids correspond to non-cyclical environmental stressful periods (such as drought, fires or flooding which may have affected food availability). Despite the limitations mentioned above, this study has demonstrated the usefulness of utilizing bone histology to infer various aspect of the biology of the extinct giraffids.

ACKNOWLEDGEMENTS

We are grateful to Sarena Govender (Cenozoic palaeontology collection manager, Iziko SA Museum, Cape Town, South Africa) for providing access to the *Sivatherium* and *Giraffa* specimens, as well as to Carmen Nacarino-Meneses (Institut Català de Paleontologia Miquel Crusafont, ICP, Life History Evolution Research Group) for general assistance and many hearty discussions about bone histology. We thank two anonymous reviewers for their constructive comments that have helped to improve this manuscript. The DSI-NRF Centre of Excellence in Palaeosciences is acknowledged for postdoctoral research support to JMJ, and the NRF AOP (grant number 136510) is thanked for financial support to AC.

DATA AVAILABILITY STATEMENT

N/a.

ORCID

Juan Marcos Jannello https://orcid.org/0000-0002-3821-0586
Anusuya Chinsamy https://orcid.org/0000-0002-9786-5080

REFERENCES

Absolonová, K., Dobisíková, M., Beran, M., Zocová, J. & Velemnský, P. (2012) The temperature of cremation and its effect on the microstructure of the human rib compact bone. *Anthropologischer Anzeiger*, *69*, 439–460. Available from: https://doi.org/10.1127/0003-5548/2012/0213

Amprino, R. (1947) La structure du tissu osseux envisagée comme expression de différences dans la vitesse de l'accroissement. *Archives de Biologie*, 58, 317–330.

Amson, E., Kolb, C., Scheyer, T.M. & Sánchez-Villagra, M.R. (2015) Growth and life history of Middle Miocene deer (Mammalia, Cervidae) based on bone histology. *Comptes Rendus Palevol*, 14(8), 637–645. https://doi.org/10.1016/j.crpv.2015.07.001

Arnold, G.W., Grassia, A., Steven, D.E. & Weeldenburg, J.R. (1991) Population ecology of western grey kangaroos in a remnant of Wandoo woodland at Bakers Hill, South Western Australia. *Wildlife Research*, 18(5), 561–575.

Bhat, M.S., Chinsamy, A. & Parkington, J. (2019) Long bone histology of *Chersina angulata*: interelement variation and life history data. *Journal of Morphology*, 280, 1881–1899.

Bhat, M.S., Chinsamy, A. & Parkington, J. (2021) Histological investigation of burnt bones: a case study of angulate tortoises from the archaeological site, Diepkloof rock shelter, Western cape, South Africa. *International Journal of Osteoarchaeology*, 31(5), 1–16.

Biewener, A.A. (1983) Allometry of quadrupedal locomotion: the scaling of duty factor, bone curvature and limb orientation to body size. *Journal of Experimental Biology*, 105, 147–171.

Brain, C.K. (1993) The occurrence of burnt bones at Swartkrans and their implications for the control of fire by early hominids. In: Brain, C.K. (Ed.) *Swartkrans: a cave's chronicle of early man*. Transvaal Museum: Pretoria, pp. 229–242.

Brain, C.K. & Sillen, A. (1988) Evidence from Swartkrans cave for the earliest use of fire. *Nature*, 336, 464–466. Available from: https://doi.org/10.1038/336464a0

Brumfitt, I.M., Chinsamy, A. & Compton, J.S. (2013) Depositional environment and bone diagenesis of the mio/pliocene langebaanweg bonebed, South Africa. *South African Journal of Geology*, 116(2), 241–258. Available from: https://doi.org/10.2113/gssajg.116.2.241

Calderón, T., Demiguel, D., Arnold, W., Stalder, G. & Köhler, M. (2019) Calibration of life history traits with epiphyseal closure, dental eruption and bone histology in captive and wild red deer. *Journal of Anatomy*, 235, 205–216.

Calderón, T., Arnold, W., Stalder, G., Painer, J. & Köhler, M. (2021) Labelling experiments in red deer provide a general model for early bone growth dynamics in ruminants. *Scientific Reports*, 11(1), 14074.

Cambra-Moo, O., Nacarino-Meneses, C., Díaz-Güemes, I., Enciso, S., García, G.O., Llorente, R.L. et al. (2015) Multidisciplinary characterization of the long-bone cortex growth patterns through sheep's ontogeny. *Journal of Structural Biology*, 191, 1–9.

Castanet, J. (2006) Time recording in bone microstructures of endothermic animals; functional relationships. *Comptes Rendus Palevol*, 5, 629–636.

Castanet, J., Croci, S., Aujard, F., Perret, M., Cubo, J. & de Margerie, E. (2004) Lines of arrested growth in bone and age estimation in a small primate: *Microcebus murinus*. *Journal of Zoology*, 263, 31–39.

Cerda, I.A., Pereyra, M.E., Garrone, M., Ponce, D., Navarro, T.G., González, R. et al. (2020) A basic guide for sampling and preparation of extant and fossil bones for histological studies. *Publicación Electrónica de la Asociación Paleontológica Argentina*, 20(1), 15–28. Available from: https://doi.org/10.5710/PEAPA.07.04.2020.314

Chinsamy, A. (1990) Physiological implications of the bone histology of *Syntarsus rhodesiensis* (Saurischia: Theropoda). *Palaeontogia Africana*, 27, 77–82.

Chinsamy, A., Angst, D., Canoville, A. & Göhlich, U.B. (2020) Bone histology yields insights into the biology of the extinct elephant birds (Aepyornithidae) from Madagascar. *Biological Journal of the Linnean Society*, 130(2), 268–295. Available from: https://doi.org/10.1093/biolinnean/blaa013

Chinsamy, A. & Hurum, J. (2006) Bone microstructure and growth patterns of early mammals. *Acta Palaeontologica Polonica*, 51, 325–338.

Chinsamy, A. & Raath, M.A. (1992) Preparation of fossil bone for histological examination. *Palaeontologia Africana*, 29, 39–44.

Chinsamy, A. & Warburton, N. (2021) Ontogenetic growth and the development of a unique fibrocartilage entheses in *Macropus fuliginosus*. *Zoology*, 144, 125860. Available from: https://doi.org/10.1016/j.zool.2020.125860

Chinsamy-Turan, A. (2005) *The microstructure of dinosaur bone: deciphering biology with fine-scale techniques*. Baltimore, Maryland: John Wiley & Sons.

Chinsamy-Turan, A. (2012) The microstructure of bones and teeth of nonmammalian therapsids. *Forerunners of Mammals: Radiation, Histology, Biology*, 2, 65–90.

Currey, J. (2002) Bones. *Structure and Mechanics*, 1, 1–380.

de Margerie, E., Cubo, J. & Castanet, J. (2002) Bone typology and growth rate: testing and quantifying 'Amprino's rule' in the mallard (*Anas platyrhynchos*). *Comptes Rendus Biologies*, 325, 221–230.

de Margerie, E., Robin, J.P., Verrier, D., Cubo, J., Groscolas, R. & Castanet, J. (2004) Assessing a relationship between bone microstructure and growth rate: a fluorescent labelling study in the king penguin chick (*Aptenodytes patagonicus*). *Journal of Experimental Biology*, 207, 869–879.

Dumont, M., Borbely, A., Kaysser-Pyzalla, A. & Sander, P.M. (2014) Long bone cortices in a growth series of *Apatosaurus sp.* (Dinosauria: Diplodocidae): geometry, body mass, and crystallite orientation of giant animals. *Biological Journal of the Linnean Society*, 112(4), 782–798.

Ellingham, S.T.D., Thompson, T.J.U., Islam, M. & Taylor, G. (2015) Estimating temperature exposure of burnt bone. A methodological review. *Science and Justice*, 55, 181–188. Available from: https://doi.org/10.1016/j.scijus.2014.12.002

Enlow, D. H. (1963). Principles of bone remodeling: an account of postnatal growth and remodeling processes in long bones and the mandible (No. 531). Thomas.

Enlow, D.H. & Brown, S.O. (1958) A comparative histological study of fossil and recent bone tissues, Part III. *The Texas Journal of Science*, 10, 187–230.

Erickson, G.M. (2005) Assessing dinosaur growth patterns: a microscopic revolution. *Trends in Ecology & Evolution*, 20, 677–684.

Fairgrieve, S.I. (2008) *Forensic cremation: recovery and analysis*. Boca Raton, FL: CRC Press, Taylor and Francis Group, pp. 148–156.

Foote, J.S. (1916) A contribution to the comparative histology of the femur. Smithsonian Institution, Vol. 35, 3.

Francillon-Vieillot, H., de Buffrénil, V., Castanet, J., Géraudie, J., Meunier, F., Sire, J. et al. (1990) Microstructure and mineralization of vertebrate skeletal tissues. In: *Skeletal biomineralization: patterns, processes and evolutionary trends*, Vol. 1, pp. 471–530. New York: Van Nostrand Reinhold.

Franz-Odendaal, T., Chinsamy, A. & Lee-Thorpe, J. (2004) High prevalence of enamel hypoplasia in an early Pliocene giraffid (*Sivatherium hendeyi*) from South Africa. *Journal of Vertebrate Paleontology*, 24(1), 235–244.

Hanson, M. & Cain, C.R. (2007) Examining histology to identify burned bone. *Journal of Archaeological Science*, 34, 1902–1913. Available from: https://doi.org/10.1016/j.jas.2007.01.009

Harris, J.M. (1976) Pleistocene Giraffoidea (Mammalia, Artiodactyla) from East Rudolf, Kenya. *Fossil Vertebrate Africana*, 4, 283–332.

Hendey, Q.B. (1981) Palaeoecology of the late tertiary fossil occurrences in 'E' quarry, Langebaanweg, South Africa, and a reinterpretation of their geological context. *Annals of the South African Museum*, 84, 1–104.

Hendey, Q.B. (1982) *Langebaanweg: a record of past life*. Cape Town: South African Museum.

Hendey, Q.B. (1989) *Langebaanweg: a record of past life*. Cape Town: South African Museum.

Herrmann, B. (1976) Neure ergebnisse zur beurteilung menschlicher brandknochen. *Zeitschrift für Rechtsmedizin*, 77, 191–200. Available from: https://doi.org/10.1007/BF02114348

Herrmann, B. (1977) On histological investigations of cremated human remains. *Journal of Human Evolution*, 6, 101–103. Available from: https://doi.org/10.1016/S0047-2484(77)80112-7

Houssaye, A., Martin Sander, P. & Klein, N. (2016) Adaptive patterns in aquatic amniote bone microanatomy–more complex than previously thought. *Integrative and Comparative Biology*, 56, 1349–1369.

Jordana, X., Marín-Moratalla, N., Moncunill-Solé, B., Nacarino-Meneses, C. & Köhler, M. (2016) Ontogenetic changes in the histological features of zonal bone tissue of ruminants: a quantitative approach. *Comptes Rendus Palevol*, 15, 255–266.

Kalsbeek, N. & Richter, J. (2006) Preservation of burned bones: an investigation of the effects of temperature and pH on hardness. *Studies in Conservation*, 51, 123–138. Available from: https://doi.org/10.1179/sic.2006.51.2.123

Klein, N. (2010) Long bone histology of Sauropterygia from the lower Muschelkalk of the Germanic Basin provides unexpected implications for phylogeny. *PLoS One*, 5(7), e11613.

Klein, R.G. (1981) Ungulate mortality and sedimentary facies in the late tertiary Varswater formation, Langebaanweg, South Africa. *Annals of the South African Museum*, 81, 233–254.

Klevezal, G. (1996) *Recording structures of mammals: determination of age and reconstruction of life history*. Rotterdam: AA Balkema.

Köhler, M., Marín-Moratalla, N., Jordana, X. & Aanes, R. (2012) Seasonal bone growth and physiology in endotherms shed light on dinosaur physiology. *Nature*, 487, 358–361.

Köhler, M. & Moyà-Solà, S. (2009) Physiological and life history strategies of a fossil large mammal in a resource-limited environment. *Proceedings of the National Academy of Sciences*, 106, 20354–20358.

Kolb, C., Scheyer, T.M., Lister, A.M., Azorit, C., De Vos, J., Schlingemann, M.A. et al. (2015) Growth in fossil and extant deer and implications for body size and life history evolution. *BMC Evolutionary Biology*, 15, 19.

Kolb, C., Scheyer, T.M., Veitschegger, K., Forasiepi, A.M., Amson, E., van Der Geer, A.A. et al. (2015) Mammalian bone palaeohistology: a survey and new data with emphasis on Island forms. *PeerJ*, 3, e1358.

Linnaeus C. 1758. *Systema natura*. Vol. 1, 10th ed, 66. Stockholm: Holmiae.

Marín-Moratalla, N., Jordana, X. & Köhler, M. (2013) Bone histology as an approach to providing data on certain key life history traits in mammals: implications for conservation biology. *Mammalian Biology*, 78, 422–429.

Moncunill-Solé, B., Orlandi-Oliverasa, G., Jordanaa, X., Rookb, L. & Köhler, M. (2016) First approach of the life history of Prolagus apricenicus (Ochotonidae, Lagomorpha) from Terre Rosse sites (Gargano, Italy) using body mass estimation and paleohistological analysis. *Comptes Rendus Palevol*, 15(1), 235–245. Available from: https://doi.org/10.1016/j.crpv.2015.04.004

Montoya-Sanhueza, G., Bennett, N.C., Oosthuizen, M.K., Dengler-Crish, C.M. & Chinsamy, A. (2020) Long bone histomorphogenesis of the naked mole-rat: histodiversity and intraspecific variation. *Journal of Anatomy*, 238, 1259–1283. Available from: https://doi.org/10.1111/joa.13381

Montoya-Sanhueza, G. & Chinsamy, A. (2017) Long bone histology of the subterranean rodent *Bathyergus suillus* (Bathyergidae): ontogenetic pattern of cortical bone thickening. *Journal of Anatomy*, 230, 203–233.

Montoya-Sanhueza, G., Šaffa, G., Šumbera, R., Chinsamy, A., Jarvis, J.U.M. & Bennett, N.C. (2022) Fossorial adaptations in African mole-rats (Bathyergidae) and the unique appendicular phenotype of naked mole-rats. *Communications Biology*, 5, 526. Available from: https://doi.org/10.1038/s42003-022-03480-z

Mori, R., Kodaka, T., Soeta, S., Sato, J., Kakino, J., Hamato, S. et al. (2005) Preliminary study of histological comparison on the growth patterns of long-bone cortex in young calf, pig, and sheep. *Journal of Veterinary Medical Science*, 67, 1223–1229.

Nacarino-Meneses, C. & Chinsamy, A. (2021) Mineralized-tissue histology reveals protracted life history in the Pliocene three-toed horse

from Langebaanweg (South Africa). *Zoological Journal of the Linnean Society*, 196, 1117–1137 in press.

Nacarino-Meneses, C., Chinsamy, A., Mayda, S., Kaya, T. & Erismis, U. (2021) Bone histology, palaeobiology, and early diagenetic history of extinct equids from Turkey. *Quaternary Research*, 100, 240–259. Available from: https://doi.org/10.1017/qua.2020.87

Nacarino-Meneses, C., Jordana, X. & Köhler, M. (2016a) Histological variability in the limb bones of the Asiatic wild ass and its significance for life history inferences. *PeerJ*, 4, e2580.

Nacarino-Meneses, C., Jordana, X. & Köhler, M. (2016b) First approach to bone histology and skeletochronology of Equus hemionus. *Comptes Rendus Palevol*, 15, 267–277.

Nacarino-Meneses, C. & Köhler, M. (2018) Limb bone histology records birth in mammals. *PLoS One*, 13, e0198511.

Nelson, R. (1992) A microscopic comparison of fresh and burned bone. *Journal of Forensic Sciences*, 37, 1055–1060. Available from: https://doi.org/10.1520/JFS13291J

O'Connor, D., Stacy-Dawes, J., Muneza, A., Fennessy, J., Gobush, K., Chase, M.J. et al. (2019) Updated geographic range maps for giraffe, Giraffa spp., throughout sub-Saharan Africa, and implications of changing distributions for conservation. *Mammal Review*, 49(4), 285–299. Available from: https://doi.org/10.1111/mam.12165

Padian, K. & Lamm, E.T. (2013) *Bone histology of fossil Tetrapods: advancing methods, analysis, and interpretation*. Berkeley: CA, University of California Press.

Ponton, F., Elżanowski, A., Castanet, J., Chinsamy, A., de Margerie, E., de Ricqlès, A. et al. (2004) Variation of the outer circumferential layer in the limb bones of birds. *Acta Ornithologica*, 39, 137–140.

Quiralte MV. 2011. *Historia evolutiva de los rumiantes (Mammalia, Artiodactyla) del Mioceno inferior de las cuencas centrales ibéricas*. Unpublished D. Thesis, Universidad Autónoma de Madrid. Madrid, Spain.

Rabe, C., Chinsamy, A. & Valenciano, A. (2022) Taxonomic and palaeobiological implications of a large, pathological sabretooth (Carnivora, Felidae, Machairodontinae) from the lower Pliocene of South Africa. *Papers in Palaeontology*, e1463. Available from: https://doi.org/10.1002/spp2.1463

Reid, R. (1996) Bone histology of the Cleveland-Lloyd dinosaurs and of dinosaurs in general, part I: introduction: introduction to bone tissues. *Brigham Young University Geology Studies*, 41, 25–72.

Reidsma, F.H., van Hoesel, A., van Os, B.J., Megens, L. & Braadbaart, F. (2016) Charred bone: physical and chemical changes during laboratory simulated heating under reducing conditions and its relevance for the study of fire use in archaeology. *Journal of Archaeological Science Reports*, 10, 282–292. Available from: https://doi.org/10.1016/j.jasrep.2016.10.001

Rios, M., Danowitz, M. & Solounias, N. (2016) First comprehensive morphological analysis on the metapodials of Giraffidae. *Palaeontologia Electronica*, 19.3.52A, 1–39.

Sanders, P.M. & Andrassi, P. (2006) Ines of arrested growth and long bone histology in Pleistocene large mammals from Germany: what do they tell us about dinosaur physiology? *Palaeontographica A*, 277(1–6), 143–159.

Schucht, P.J., Klein, N. & Lambertz, M. (2021) What's my age again? On the ambiguity of histology-based skeletochronology. *Proceedings of the Royal Society B*, 288, 20211166. Available from: https://doi.org/10.1098/rspb.2021.1166

Shipman, P., Foster, G. & Schoeninger, M. (1984) Burnt bones and teeth: an experimental study of color, morphology, crystal structure and shrinkage. *Journal of Archaeological Science*, 11(4), 307–325. Available from: 10.1016/0305-4403(84)90013-X

Shorrocks, B. (2016) *The giraffe: biology, ecology, evolution and behaviour*. Heslington, York, UK: John Wiley & Sons.

Singh, I., Tonna, E. & Gandel, C. (1974) A comparative histological study of mammalian bone. *Journal of Morphology*, 144, 421–437.

Skedros, J.G., Sorenson, S.M. & Jenson, N.H. (2007) Are distributions of secondary osteon variants useful for interpreting load history in mammalian bones? *Cells, Tissues, Organs*, 185, 285–307.

Skedros, J.G., Su, S.C. & Bloebaum, R.D. (1997) Biomechanical implications of mineral content and microstructural variations in cortical bone of horse, elk, and sheep calcanei. *The Anatomical Record*, 249, 297–316.

Skedros, J.G., Sybrowsky, C.L., Parry, T.R. & Bloebaum, R.D. (2003) Regional differences in cortical bone organization and microdamage prenacarinoe in Rocky Mountain mule deer. *Part A: Discoveries in Molecular, Cellular, and Evolutionary Biology*, 274, 837–850.

Smith, C. C. D. 2020. *Giraffa camelopardalis: limb bone histology through ontogeny*. Unpublished Master Thesis, University of Cape Town, Cape Town, South Africa.

Solounias, N. (2007) Family Giraffidae. In: Prothero, D.R. & Foss, S.E. (Eds.) *The evolution of artiodactyls*. Baltimore, MD: Johns Hopkins University Press, pp. 257–277.

Taylor, R.E., Hare, P.E. & White, T.D. (1995) Geochemical criteria for thermal alteration of bone. *Journal of Archaeological Science*, 22, 115–119. Available from: 10.1016/S0305-4403(95)80169-3

Ubelaker, D.G. (2009) The forensic evaluation of burned skeletal remains: A synthesis. *Forensic Science International*, 183, 1–5. Available from: 10.1016/j.forsciint.2008.09.019

Valenciano, A., Morales, J. & Govender, R. (2022) Eucyon khoikhoi sp. nov. (Carnivora: Canidae) from Langebaanweg 'E'Quarry (Early Pliocene, South Africa): the most complete African canini from the Mio-Pliocene. *Zoological Journal of the Linnean Society*, 194(2), 366–394. Available from: https://doi.org/10.1093/zoolinnean/zlab022

van Hoesel, A., Reidsma, F. H., van Os, B. J. H., Megens, L., & Braadbaart, F. (2019). Combusted bone: Physical and chemical changes of bone during laboratory simulated heating under oxidising conditions and their relevance for the study of ancient fire use. *Journal of Archaeological Science: Reports*, 28, 102033. https://doi.org/10.1016/j.jasrep.2019.102033

van Schalkwyk, O.L., Skinner, J.D. & Mitchell, G. (2004) A comparison of the bone density and morphology of giraffe (*Giraffa camelopardalis*) and buffalo (*Syncerus caffer*) skeletons. *Journal of Zoology*, 264, 307–315.

Woolley, M.R., Chinsamy, A., Govender, R. & Bester, M.N. (2019) Microanatomy and histology of bone pathologies of extant and extinct phocid seals. *Historical Biology*, 1–16.

How to cite this article: Jannello, J.M. & Chinsamy, A. (2023) Osteohistology and palaeobiology of giraffids from the Mio–Pliocene Langebaanweg (South Africa). *Journal of Anatomy*, 00, 1–19. Available from: https://doi.org/10.1111/joa.13825